

Electric Control of Polarity in Spin-Orbit Josephson Diode

Junghyun Shin¹, Jae-Ho Han^{2,3}, Anjali Rathore⁴, Joon Sue Lee⁴,
Seung-Bo Shim⁵, Jinwoong Cha⁵, Sunghun Park^{3*}, Junho Suh^{1*}

¹Department of Physics, Pohang University of Science and Technology (POSTECH),
Pohang, South Korea.

²Department of Physics, Korea Advanced Institute of Science and Technology
(KAIST), Daejeon, South Korea.

³Center for Theoretical Physics of Complex Systems, Institute of Basic Science,
Daejeon, South Korea.

⁴Department of Physics and Astronomy, University of Tennessee, Knoxville,
Tennessee, USA.

⁵Quantum Technology Institute, Korea Research Institute of Standards and Science,
Daejeon, South Korea.

*Corresponding author(s). E-mail(s): sunghun.park@ibs.re.kr,
junhosuh@postech.ac.kr;

Abstract

The Josephson diode effect (JDE), characterized by a unidirectional supercurrent across a Josephson junction, arises from non-reciprocal critical currents typically controlled by magnetic fields. In this study, we demonstrate JDE controlled by local electric fields, achieving complete polarity reversal through gate voltages on epitaxial Al-InAs Josephson junctions. Our observations reveal intricate effects of in-plane magnetic fields and gate voltages on the JDE. We develop a theoretical model that considers the coherent interplay between finite Cooper-pair momentum (fCPM) and anisotropic spin-orbit coupling (SOC), identifying that fCPM dominates JDE at low in-plane magnetic fields, while SOC governs its polarity reversal at high fields. This model aligns well with experimental data, illustrating precise electric control of JDE polarity through anisotropic SOC. These findings introduce a novel approach to controlling superconducting circuits, paving a route toward advanced applications in superconducting quantum devices.

1 Main

Non-reciprocal semiconductor devices, which allow selective electric current flow, are central to modern electronics. As the importance of dissipation-free electronics increases, non-reciprocal superconducting devices have gathered keen interest due to their potential application [1–7]. Theoretically, the simultaneous breaking of time-reversal and inversion symmetries enables non-reciprocal supercurrents. A prominent approach to achieving this is through superconducting hybrid systems, such as Josephson junctions (JJs) lacking inversion symmetry [4–6, 8]. Unidirectional supercurrent, or Josephson diode effect (JDE), can be achieved by the non-reciprocal critical currents when applying magnetic field. Magnetic field acts as a crucial vector parameter in non-reciprocal mechanisms [9–12], and also changes the characteristics of superconducting systems [13, 14], thereby enabling control over the polarity of the JDE.

JJs fabricated on epitaxially grown Al-InAs possess several advantageous properties [15–17], such as strong spin-orbit coupling (SOC), a large g -factor, and a hard proximity-induced gap, making them excellent platforms for studying the JDE. Previous studies on DC transport, inductance measurements, and tunneling spectroscopy have reported the magnetic field-driven JDE [4, 18–22], with a signature of sign-reversal at finite magnetic fields. Proposed mechanisms [9, 11] for the observed JDE focus on two distinct origins: strong Rashba SOC and the finite Cooper-pair momentum (fCPM) arising from orbital effects.

In this work, we investigate supercurrent transports in an Al-InAs heterostructure-based superconducting quantum interference device (SQUID) to identify electric field as a new route to manipulate its non-reciprocity. Notably, local electric fields applied onto the JJs control JDE efficiently up to the point to induce polarity reversal. Through SQUID oscillations, we examine the asymmetry of the current-phase relation (CPR) related to the polarity of the JDE. By increasing an in-plane magnetic field, we observe the polarity reversal of the JDE with strong dependence on the gate voltages over JJs. Our theoretical model attributes the polarity reversal to the coherent interplay between fCPM from orbital effects and anisotropic SOC, including Rashba and Dresselhaus SOCs. At low magnetic fields, the JDE is primarily influenced by fCPM. Conversely, at higher magnetic fields, the SOC-assisted mechanism becomes the dominant factor in determining the JDE’s polarity, which is tunable electrically by adjusting the gate voltage.

2 Device

Our device is a DC SQUID fabricated with an Al-InAs heterostructure (Figs. 1a-b). The heterostructure consists of an InAs quantum well topped by a 10-nm-thick InGaAs barrier, covered by a 6-nm-thick Al layer (Fig. S1). The Al layer is epitaxially grown without breaking vacuum to provide a clean proximity contact to the underlying quantum well, inducing a superconducting gap in the InAs layer comparable to that of the Al layer [15, 16]. The SQUID comprises two planar superconductor-normal-superconductor (SNS) JJs, denoted as J1 and J2 respectively, which are realized by removing strips of the Al layer (See details in Methods). Both junctions have the nominal junction length of 100 nm (L_j), the junction width of 4.5 μm (W), and the superconducting lead length of 1.4 μm (L_s). Each junction is controlled by a corresponding top gate, with voltages V_{g1} and V_{g2} , respectively, affecting Rashba SOC strength and carrier density (Supplementary Information). The DC bias current (I_{DC}) flows parallel to the [110] crystallographic direction of the InAs layer. Magnetic fields are applied along y - (in-plane; B_y) and z -direction (out-of-plane; B_z), and the enclosed area of the SQUID loop (A_{SQUID}) is 20 μm^2 (Fig. 1b). A large B_y up to 200 mT is employed to break time-reversal symmetry, while sub-mT B_z is used to adjust the external flux passing through the SQUID loop.

3 CPRs and SQUID oscillations with JDE

A general form of CPRs in JJs is given by $I(\varphi) = \sum_{n=1}^{\infty} a_n \sin(n\varphi + \varphi_n)$, where I is current, φ is the superconducting phase difference across the junction, and a_n and φ_n are the amplitude and the phase offset in the n -th order harmonic, respectively [23, 24]. To illustrate the concept of non-reciprocal critical currents, it suffices to consider up to the second harmonic [5, 6],

$$I(\tilde{\varphi}) = a_1 \sin(\tilde{\varphi}) + a_2 \sin(2\tilde{\varphi} + \delta), \quad (1)$$

where $\tilde{\varphi} = \varphi + \varphi_1$, $\delta = \varphi_2 - 2\varphi_1$. The anomalous phase difference δ determines the polarity of the JDE. Assuming $0 \leq \delta < 2\pi$, at $\delta = 0$ or π , the CPR is anti-symmetric about $\tilde{\varphi} = 0$ (Fig. 1c). When $0 < \delta < \pi$, I_c^+ is smaller than I_c^- , where I_c means a critical current and their superscripts + and - denote forward and backward directions. Conversely, when $\pi < \delta < 2\pi$, I_c^+ is larger than I_c^- . A representative CPR with JDE is shown as the orange

solid line in Fig. 1c, with $\delta = \pi/2$ and $a_2/a_1 = 0.2$. In this case, Josephson diode efficiency, defined as $(I_c^+ - I_c^-)/(I_c^+ + I_c^-)$, is -0.2 .

When JJs form a SQUID, the shape of the oscillating SQUID critical current is determined by their CPRs, while the period is dictated by the effective area of the SQUID loop. Figure 1d presents representative SQUID oscillations of forward and backward critical currents, assuming both JJs are identical. Their CPRs correspond to those shown in Fig. 1c. In case of the asymmetric CPR, the amplitudes of the SQUID oscillations differ between two polarities, leading to non-reciprocal critical currents in the SQUID. The peak heights, denoted as peak currents I_p^+ and I_p^- , correspond to points of maximum constructive interference, which is the sum of the critical currents of the two JJs for the corresponding direction. We quantify the non-reciprocity in SQUID peak currents as $\eta = (I_p^+ - I_p^-)/(I_p^+ + I_p^-)$. This efficiency is the same as the Josephson diode efficiency of the two identical JJs under the same gate voltages V_g . The direction-dependent amplitudes of peak currents stem from the non-reciprocity in the composing JJs, thus distinct from non-reciprocal supercurrents in SQUIDs relying on interferences between non-identical JJs [25, 26] (Supplementary Information).

4 JDE and asymmetry of the CPR

We measure differential resistance (dV/dI) as a function of B_z and I_{DC} at $B_y = 33$ mT and $V_g = 0$ (Fig. 2a-b). While the critical currents oscillate with a fixed period of 42 μ T (Fig. 2a), the magnitude of the critical current depends on the current direction (Fig. 2b). The difference between I_c^+ and I_c^- is most pronounced near the peak currents, with I_c^- being larger than I_c^+ (Fig. 2c). This is attributed to the JDE in the composing JJs, resulting in unidirectional supercurrents when the current amplitude falls within the range between I_c^+ and I_c^- (Supplementary Information).

Figure 2d shows I_c^+ and I_c^- near $\Phi_{ex} = 0$ at various B_y , normalized by the average peak current I_p^{avg} for each B_y . In the absence of JDE, both I_c^+ and I_c^- are expected to be equal to I_p^{avg} at $\Phi_{ex} = 0$. However, we observe that I_c^+ and I_c^- at $\Phi_{ex} = 0$ show modulation with respect to B_y in opposite directions. In addition, the polarity of the non-reciprocal critical currents changes over B_y , reversing at $B_y = 0$ and $B_y \approx \pm 55$ mT. We note that the polarity reversal at finite magnetic field implies non-trivial mechanisms governing JDE

in our device as the field strength is significantly lower than that observed in previous experiments, within the 220–400 mT range [19, 21, 22].

Figure 3a presents the Josephson diode efficiency η as a function of B_y , which is obtained from the data shown in Fig. 2d. η is anti-symmetric with respect to B_y , consistent with the Onsager-Casimir relations [21, 27]. In addition, the diode efficiency displays strong dependence on B_y in a non-monotonic way. Notably, it increases linearly from $B_y = 0$, decreases beyond 33 mT, and reverses sign beyond 55 mT. This polarity-reversed diode efficiency peaks around $B_y = 100$ mT and gradually diminishes with further increase in B_y . The magnitude of η reaches maximum at approximately 0.04, reaching 0.02 after polarity reversal. This intricate relation between the observed η and B_y is at the focus of our study.

We investigate the relation between the anomalous phase difference δ (Eq. (1)) and the diode efficiency η by fitting the measured SQUID oscillations at each B_y with a numerically calculated SQUID oscillation (Fig. 3b and Supplementary Information). The extracted δ is plotted in Fig. 3a, demonstrating a direct correlation with the diode efficiency. η is negative for $0 < \delta < \pi$, and it is positive for $\pi < \delta < 2\pi$, thus polarity reversal of diode efficiency coincides with $\delta = \pi$. This correspondence between δ and η implies the existence of higher harmonics in CPR (Eq. (1)).

5 Spin-orbit interaction origin of sign reversal

We develop a model to provide quantitative explanation of measured JDE in our device considering both anisotropic SOC and fCPM. Rashba and Dresselhaus SOC in an Al-InAs quantum well arise from the lack of inversion symmetry. Rashba SOC arises from the electric field in an asymmetric quantum well and can be controlled by an external electric field perpendicular to the InAs layer, while Dresselhaus SOC arises from an intrinsic electric field within the crystal lattice lacking inversion symmetry. In our device, the current flows along the [110] direction leading to an anisotropic SOC owing to the coexistence of Rashba and Dresselhaus SOC [18]. Additionally, when applying B_y , Cooper pairs acquire fCPM due to the orbital effect [9]. In the vector potential $\mathbf{A} = B_y z \hat{x}$, parallel to the interfaces of the superconductor ($z = d$) and the semiconductor ($z = 0$), the orbital effect leads to the fCPM, $q = -\pi B_y d / \Phi_0$. While the Zeeman effect with SOC [10, 28, 29] also leads to fCPM, it is estimated to be three orders of magnitude smaller than the orbital effect when using realistic parameter values and thus is neglected in our model (Supplementary Information).

fCPM decreases and eventually closes the proximity-induced gap at $B_y = B_g = \Delta/(ev_F d)$ due to the Doppler shift of Bogoliubov quasiparticle energy $\Delta \pm \hbar v_F q$ [9]. The B_y dependence of I_p^{avg} supports the crucial role of the fCPM in the transport characteristics of the JJs. I_p^{avg} gradually decreases with increasing B_y , becoming approximately half near 55 mT. This behavior is reproduced when the fCPM is included in the model, regardless of the presence of SOC (inset of Fig. 4a).

To verify the interplay between SOC and fCPM quantitatively, we fit the B_y dependence of the efficiency η by varying the chemical potential μ , the junction transparency τ and the Rashba SOC α , with constant Dresselhaus SOC β (Fig. 4a). From the best fit, our estimate of B_g is about 33 mT with induced superconducting gap $\Delta = 170 \mu\text{eV}$ and $v_F = 5.1 \times 10^5 \text{ m}\cdot\text{s}^{-1}$. Details of fitting parameters are summarized in Methods. The relative importance of SOC and fCPM becomes evident as we compare our model to an alternative one without SOC. In the low-field region of $B_y < B_g$, η from the SOC-free model also follows the data closely, indicating that the fCPM dominates JDE at low fields below B_g . In contrast, the SOC-free model does not explain the polarity reversal at high fields, demonstrating the crucial contribution of SOC to JDE. The importance of SOC in polarity reversal is also evidenced by the anomalous phase difference δ . In Fig. 4b, δ from our SOC-assisted and SOC-free model diverge significantly at $B_y > B_g$. δ saturates at $\pi/2$ in the SOC-free model, whereas the SOC-assisted model predicts that δ does not saturate at $\pi/2$ and eventually reaches the opposite-polarity region, transitioning from $0 < \delta < \pi$ to $\pi < \delta < 2\pi$.

In order to address the SOC effect on JDE in more detail, we analyze two different types of transverse modes, spin-degenerate modes (SDM) and spin-split modes (SSM) on the Fermi surfaces with spin-orbit splitting (Fig. 4c). Importantly, SSM is eminent in the polarity reversal in JDE (Fig. 4d). The phase shifts induced by SDM reproduce δ obtained from the SOC-free model. Both φ_1 and φ_2 , the first- and second-order phase shifts, approach $-\pi/2$ with increasing B_y , leading to the saturation of $\delta = \pi/2$ and the absence of the polarity reversal. In contrast, the contribution of SSM advances δ further to cross π , due to the spin-orbit effect on φ_2 , resulting in the polarity reversal.

The analysis of SDM and SSM reveals that the emergence of the polarity reversal depends on the anisotropy of the SOC. The Andreev spectra of the SDM and SSM evolve differently with B_y . While the SDM exhibits Zeeman-like level splitting, the SSM shows a phase shift in its Andreev spectrum relative to that of the SDM. The distinct evolution

with B_y produces higher harmonics in the total CPR. For Rashba-only SOC, this effect is weak as the SSM is only a small fraction of the total number of channels, on the order of $k_{\text{SOC}}/k_F \ll 1$, and do not affect the higher harmonics. Here, $k_{\text{SOC}} = 2m^*\alpha/\hbar^2$ and k_F are the wavevector splitting due to the SOC and the Fermi wavevector, respectively. However, the anisotropic SOC, with comparable α and β , enhances the amplitude of CPR of the SSM to make it comparable to the second harmonics of SDM in the SOC-assisted regime (Supplementary Information). Thus SSM can produce significant contribution to the phase shift φ_2 , and δ crosses π to result in the reversal of JDE polarity.

Previously reported polarity reversal in Al-InAs JJs was explained by a $0-\pi$ transition driven by the Zeeman energy [13, 19] or a topological phase transition [21]. The former mechanism arises at $|g\mu_B B_y|/2 \approx \hbar v_F/L_j$ from which we estimate $B_y \approx 6.9$ T, much higher than the field strength in our experiments [19]. In addition, the B_y dependence of the critical current of J2, while J1 is almost pinched off (Supplementary Information) does not show the signature of the topological phase transition — the suppression and revival of the critical current [30] — ruling out the possibility of topological transition in our experiments.

6 Gate-voltage control of JDE

The anisotropic SOC with both Rashba and Dresselhaus effect results in the emergence JDE sign-reversal at high in-plane magnetic fields. In our device, the Rashba SOC strength can be controlled by varying the gate voltage, enabling tuning of the SOC characteristics in the InAs layer. By adjusting V_g from -6V to 0V, we obtained the B_y dependence of η and δ (Fig. 5a and Extended Data Fig. 1a), demonstrating the evolution from the $\pi/2$ -saturation to the π -crossing behavior, along with the emergence of high-field sign-reversal. Gate voltage leads to distinct effects in the fCPM-dominated regime at low fields and the SOC-assisted region at high fields. The fCPM-dominated regime at $B_y < B_g$ is nearly independent of V_g , while the SOC-assisted regime at $B_y > B_g$ is highly adjustable by V_g . Figures 5b and 5c illustrate the V_g dependence at two selected fields, 22 mT and 66 mT, representing the two distinct regimes. At $B_y = 22$ mT, δ is weakly dependent on V_g , with $\eta \approx -0.04$. Conversely, at $B_y = 66$ mT, δ is strongly affected by V_g , exhibiting π -crossing at $V_g \approx -3$ V, with η varying from approximately -0.03 to 0.01 .

To assess the effect of gate voltages to our model calculations, we gradually decrease the chemical potential as V_g decreases and adjust τ and α , respectively. The resulting fits exhibit

excellent agreement with the experimental data at both zero and finite gate-voltages (Fig. 5a and Extended Data Fig. 1b), both in the efficiency η and the anomalous phase difference δ . Such agreement confirms that the observed polarity reversal, which is controllable using the gate voltage or the magnetic field, results from the coherent interplay between SOC and fCPM.

7 Conclusions

In conclusion, we demonstrate electric control of JDE with high tunability to the extent that its polarity is reversed. This controllability of JDE is provided by adjusting gate voltages under in-plane magnetic field perpendicular to the supercurrents. Our theoretical model shows that the higher harmonics of JJ CPR determines this polarity reversal. Detailed analysis of multichannel contributions to the CPR reveals that the gate-voltage induced changes of spin-orbit anisotropy perturb the higher harmonics of the CPR, affecting the JDE polarity as a result. At the point of polarity reversal where JDE becomes zero, the device behaves as if Rashba SOC effectively recovers the broken symmetries. Our device is compatible with superconducting quantum circuit architectures [31] and its locally tunable nonreciprocity could lead to novel applications in superconducting electronic devices.

8 Methods

Characteristics of InAs heterostructure

The Al-InAs heterostructure is grown on a semi-insulating InP substrate by molecular beam epitaxy. The heterostructure consists of a 100 nm $\text{In}_{0.52}\text{Al}_{0.48}\text{As}$ matched buffer, 25 nm $\text{In}_{0.52}\text{Al}_{0.48}\text{As}/\text{In}_{0.52}\text{Ga}_{0.48}\text{As}$ superlattice, 800 nm $\text{In}_x\text{Al}_{1-x}\text{As}$ graded buffer ($x = 0.52$ to 0.81), 25 nm $\text{In}_{0.81}\text{Al}_{0.19}\text{As}/\text{In}_{0.75}\text{Ga}_{0.25}\text{As}$ superlattice, 106 nm $\text{In}_{0.81}\text{Al}_{0.19}\text{As}$ the topmost buffer layer, a 4-nm-thick $\text{In}_{0.75}\text{Ga}_{0.25}\text{As}$ bottom barrier, a 7 nm InAs quantum well, a 10 nm $\text{In}_{0.75}\text{Ga}_{0.25}\text{As}$ top barrier, and 6 nm aluminum film as a superconducting layer. A Si- δ -doping layer with a sheet density of $1.4 \times 10^{12} \text{ cm}^{-2}$ is placed 6 nm below the top surface of the buffer layer.

We perform a characterization of the InAs quantum well in a top-gated Hall-bar geometry device where the top Al layer is removed. The characterization of the quantum well reveals a peak mobility of $2.2 \times 10^4 \text{ cm}^2/\text{Vs}$ at an electron sheet density of $1.1 \times 10^{12} \text{ cm}^{-2}$, corresponding to an electron mean free path $l_e \approx 380 \text{ nm}$. A conductance peak emerges

near $B_z = 0$ due to the weak anti-localization effect. By fitting the weak anti-localization signal with the Iordanski, Lyanda-Geller, and Pikus (ILP) model [15, 32], we obtain the linear Rashba spin-orbit parameter $\alpha \approx 8.8$ meV nm when the gate voltage is neutral (Supplementary Information). Meanwhile, we perform a characterization of the Al layer in a Hall-bar geometry device. The zero-field transition temperature is 1.49 K and the in-plane critical magnetic field is 2.7 T at 10 mK. Using the relation $\Delta = 1.75k_B T_c$, Δ is estimated to be approximately 200 μ eV.

Fabrication

The fabrication process for the devices involves several standard electron-beam lithography steps. These include defining MESAs and Josephson junctions and depositing top gate electrodes. MESAs are isolated by a 270 nm chemical wet etch using a solution ($\text{H}_2\text{O} : \text{C}_6\text{H}_8\text{O}_7 : \text{H}_3\text{PO}_4 : \text{H}_2\text{O}_2 = 220:55:3:3$) after the local removal of Al layers using a wet etchant (Transene D). Josephson junctions on the MESAs are defined by selectively removing Al layers. Subsequently, a 20-nm-thick insulating Al_2O_x layer is deposited via atomic layer deposition. The top gate electrodes are deposited in two steps using electron-beam evaporation: 5 nm Ti and 30 nm Au deposition for fine structures, followed by a successive deposition of 10 nm Ti and 300 nm Au deposition for larger structures.

Measurements

All electrical measurements are conducted in a dilution refrigerator equipped with suitable electronic low-pass filters at the mixing chamber stage, with a base temperature of 10 mK. Two different direction magnetic fields, in-plane field B_y and out-of-plane field B_z , are applied by a superconducting magnet installed in the refrigerator and by a homemade superconducting coil attached to the lid of a sample holder, respectively.

DC current-biased differential resistance (dV/dI) measurements are performed by using standard low-frequency lock-in techniques with an excitation current $I_{ex} = 10$ nA. To obtain forward (backward) critical currents I_c^+ (I_c^-), DC bias current I_{DC} sweeps increasing (decreasing) from zero. In cases with an abrupt dV/dI jump, as shown in Fig. 2b, the current value at the abrupt resistance jump is extracted as the forward (backward) critical current. With increasing $|B_y|$ or applying negative gate voltages, the discontinuous $dV/dI(I_{DC})$ changes to a continuous curve with a dV/dI peak. We define the critical currents in the continuous curves where dV/dI reaches its maximum value. This definition is consistent with that used in Ref. [7].

Theoretical model

Given that the two planar JJs forming the SQUID device are identical, we examine a single planar JJ and calculate the Andreev level spectrum and supercurrent by solving the Bogoliubov-de Gennes (BdG) equation for the junction, $H_{\text{BdG}}\Psi = E\Psi$, in the Nambu basis $\Psi = (\psi_{e\uparrow}, \psi_{e\downarrow}, \psi_{h\downarrow}, -\psi_{h\uparrow})^T$ with excitation energy E [33]. The BdG Hamiltonian H_{BdG} reads

$$H_{\text{BdG}} = \begin{pmatrix} H_0 - \mu & \Delta(x) \\ \Delta^*(x) & -\mathcal{T}H_0\mathcal{T}^{-1} + \mu \end{pmatrix}, \quad (2)$$

where μ is the chemical potential measured from the bottom of the electron band and $\mathcal{T} = -i\sigma_y\mathcal{C}$ is the time-reversal operator with Pauli matrices σ_i ($i = x, y, z$) in spin space and complex conjugation \mathcal{C} . The electron gas with effective mass $m^* = 0.023 m_e$ is described by the electron Hamiltonian H_0 ,

$$H_0 = \frac{\hbar^2(k_x^2 + k_y^2)}{2m^*} - (\alpha + \beta)k_x\sigma_y + (\alpha - \beta)k_y\sigma_x + (V_b + E_Z\hat{\sigma}_y)L_j\delta(x). \quad (3)$$

It takes into account the Rashba α and Dresselhaus β SOCs along the crystallographic [110] direction [18, 34], the Zeeman energy $E_Z = g\mu_B B_y/2$ of the electrons in the in-plane magnetic field applied along the y -direction with g -factor $g = -17$, the potential scattering V_b . We assume that E_Z and V_b are present only at the junction region $0 < x < L_j$ and zero elsewhere. The width of the junction $W = 4 \mu\text{m}$ is much larger than $L_j = 100 \text{ nm}$. The proximity-induced superconducting pairing potential $\Delta(x)$ is given by [9]

$$\Delta(x) = \Delta e^{i2qx} [\Theta(-x) + e^{i\varphi}\Theta(x - L_j)], \quad (4)$$

where q is the orbital induced fCPM, $\Delta = 170 \mu\text{eV}$ is the proximity-induced gap and φ is the superconducting phase difference, and $\Theta(x)$ is the step function.

We consider a short junction limit $L_j \ll \xi = \hbar v_F/\Delta$. For $\mu = 17 \text{ meV}$, which is used in Fig. 4, the superconducting coherence length is $\xi = 2 \mu\text{m}$. The scattering in the junction is modeled by a delta function $\delta(x)$, as shown in Eq. (3). We focus on the regime where the chemical potential is much larger than the superconducting gap, $\mu \gg \Delta$, allowing us to neglect the normal reflection at the interface between the superconductor and the

normal region can be neglected (Andreev approximation). Our model in Eq. (2) then can be treated by linearizing the energy dispersion around μ . We impose hard-wall boundary conditions at $y = 0$ and W , which quantize the wave vector k_y as $k_m = m\pi/W$. The physical confinement along the y -direction results in multiple transverse subbands labeled by m . The choice of boundary conditions would be irrelevant in our case of $W \gg L_j$. The total Josephson current flowing across the junction in the x -direction is obtained by summing up the contributions from each transverse subband,

$$I(\varphi) = -\frac{e}{\hbar} \sum_{m=1}^M \int_0^\infty dE E \frac{\partial}{\partial \varphi} \rho_m(E, \varphi), \quad (5)$$

where $e > 0$ is the elementary charge and M is the number of transverse subbands below the chemical potential. The density of states ρ_m of the junction can be expressed in terms of the scattering matrix $s_N^{(m)}$ of the normal region and the matrix $s_A^{(m)}$ at the superconductor-normal interface as

$$\rho_m(E, \varphi) = -\frac{1}{\pi} \text{Im} \frac{\partial}{\partial E} \text{Log Det} \left[I - s_A^{(m)}(E + i\varepsilon, \varphi) s_N^{(m)}(E + i\varepsilon, \varphi) \right]. \quad (6)$$

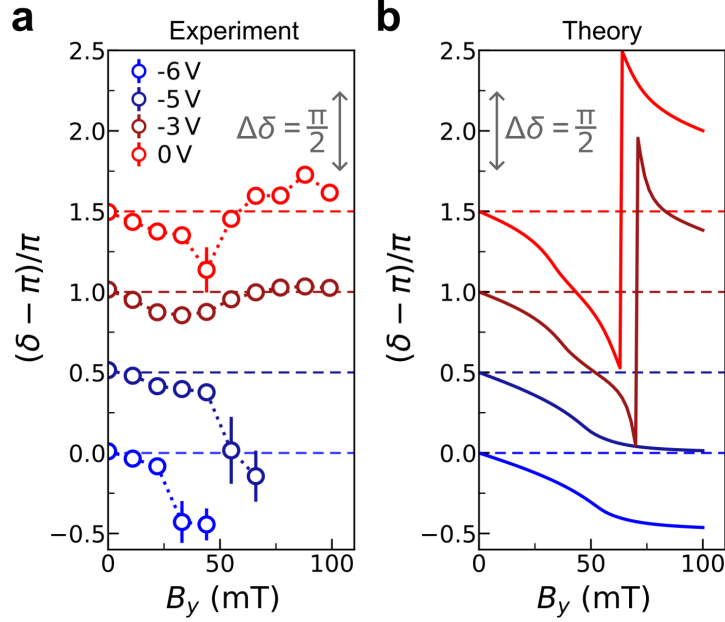
Here we introduced an infinitesimal imaginary energy ε to calculate the density of states of both the bound and continuum states of the junction. The scattering matrices $s_A^{(m)}$ and $s_N^{(m)}$ are obtained by linearizing the energy dispersion of a transverse subband for a given wave vector k_m .

Calculation parameters for Figs. 4 and 5

Theoretical results were obtained from Eq. (5). We give in Table 1 the parameters corresponding to the figures. Here, $\Delta = 170 \mu\text{eV}$ and $q = 1.42 \times 10^{-5} B_y \text{ mT}^{-1} \text{ nm}^{-1}$ are used. The transparency τ at zero field is obtained by fitting the calculated CPR with the formula of the form $I_0 \sin(\varphi) / \sqrt{1 - \tau \sin^2(\varphi/2)}$ [35].

	$\alpha(\text{meV nm})$	$\beta(\text{meV nm})$	$\mu(\text{meV})$	$V_b(\text{meV})$	$\tau(B_y = 0)$
Fig. 4a	7.53	4.23	17	2.76	0.536
Fig. 4b	0	0	17	2.76	0.515
Fig. 5 $V_g=0$	7.53	4.23	17	2.76	0.536
Fig. 5 $V_g=-3$ V	7.26	4.23	13.6	2.51	0.529
Fig. 5 $V_g=-5$ V	6.03	4.23	8.5	1.84	0.542
Fig. 5 $V_g=-6$ V	5.08	4.23	6.8	1.34	0.636

Extended Data Table 1 Parameters used for the calculations of the diode efficiency and the anomalous phase difference shown in the figures, using Eq. (5).



Extended Data Fig. 1 The evolution of δ with V_g . **a**, Variation of δ by varying V_g from -6 V to 0 V. Data are vertically offset for clarity. **b**, Variation of δ by increasing the Rashba SOC.

References

- [1] Nadeem, M., Fuhrer, M. S. & Wang, X. The superconducting diode effect. *Nat. Rev. Phys.* **5**, 558–577 (2023).
- [2] Ando, F. *et al.* Observation of superconducting diode effect. *Nature* **584**, 373–376 (2020).
- [3] Wu, H. *et al.* The field-free Josephson diode in a van der Waals heterostructure. *Nature* **604**, 653–656 (2022).
- [4] Baumgartner, C. *et al.* Supercurrent rectification and magnetochiral effects in symmetric Josephson junctions. *Nat. Nanotechnol.* **17**, 39–44 (2022).
- [5] Pal, B. *et al.* Josephson diode effect from Cooper pair momentum in a topological semimetal. *Nat. Phys.* **18**, 1228–1233 (2022).
- [6] Jeon, K.-R. *et al.* Zero-field polarity-reversible Josephson supercurrent diodes enabled by a proximity-magnetized Pt barrier. *Nat. Mater.* **21**, 1008–1013 (2022).
- [7] Lin, J.-X. *et al.* Zero-field superconducting diode effect in small-twist-angle trilayer graphene. *Nat. Phys.* **18**, 1221–1227 (2022).
- [8] Turini, B. *et al.* Josephson diode effect in high-mobility InSb nanoflags. *Nano Lett.* **22**, 8502–8508 (2022).
- [9] Davydova, M., Prembabu, S. & Fu, L. Universal Josephson diode effect. *Sci. Adv.* **8**, eabo0309 (2022).
- [10] Yuan, N. F. Q. & Fu, L. Supercurrent diode effect and finite-momentum superconductors. *Proc. Natl. Acad. Sci. USA* **119**, e2119548119 (2022).
- [11] Costa, A., Fabian, J. & Kochan, D. Microscopic study of the Josephson supercurrent diode effect in Josephson junctions based on two-dimensional electron gas. *Phys. Rev. B* **108**, 054522 (2023).
- [12] Reynoso, A. A., Usaj, G., Balseiro, C. A., Feinberg, D. & Avignon, M. Spin-orbit-induced chirality of Andreev states in Josephson junctions. *Phys. Rev. B* **86**, 214519

- (2012).
- [13] Yokoyama, T., Eto, M. & Nazarov, Y. V. Anomalous Josephson effect induced by spin-orbit interaction and Zeeman effect in semiconductor nanowires. *Phys. Rev. B* **89**, 195407 (2014).
 - [14] Lutchyn, R. M., Sau, J. D. & Das Sarma, S. Majorana fermions and a topological phase transition in semiconductor-superconductor heterostructures. *Phys. Rev. Lett.* **105**, 077001 (2010).
 - [15] Shabani, J. *et al.* Two-dimensional epitaxial superconductor-semiconductor heterostructures: A platform for topological superconducting networks. *Phys. Rev. B* **93**, 155402 (2016).
 - [16] Kjaergaard, M. *et al.* Quantized conductance doubling and hard gap in a two-dimensional semiconductor-superconductor heterostructure. *Nat. Commun.* **7**, 12841 (2016).
 - [17] Lee, J. S. *et al.* Transport studies of epi-Al/InAs two-dimensional electron gas systems for required building-blocks in topological superconductor networks. *Nano Lett.* **19**, 3083–3090 (2019).
 - [18] Baumgartner, C. *et al.* Effect of Rashba and Dresselhaus spin-orbit coupling on supercurrent rectification and magnetochiral anisotropy of ballistic Josephson junctions. *Journal of Physics: Condensed Matter* **34**, 154005 (2022).
 - [19] Costa, A. *et al.* Sign reversal of the Josephson inductance magnetochiral anisotropy and $0-\pi$ -like transitions in supercurrent diodes. *Nat. Nanotechnol.* **18**, 1266–1272 (2023).
 - [20] Reinhardt, S. *et al.* Link between supercurrent diode and anomalous Josephson effect revealed by gate-controlled interferometry. *Nat. Commun.* **15**, 4413 (2024).
 - [21] Banerjee, A. *et al.* Phase asymmetry of Andreev spectra from Cooper-pair momentum. *Phys. Rev. Lett.* **131**, 196301 (2023).

- [22] Banerfizadeh, N. *et al.* Superconducting diode effect sign change in epitaxial Al-InAs Josephson junctions. *Commun. Phys.* **7**, 120 (2024).
- [23] Golubov, A. A., Kupriyanov, M. Y. & Il'ichev, E. The current-phase relation in Josephson junctions. *Rev. Mod. Phys.* **76**, 411–469 (2004).
- [24] Willsch, D. *et al.* Observation of Josephson harmonics in tunnel junctions. *Nat. Phys.* **20**, 815–821 (2024).
- [25] Souto, R. S., Leijnse, M. & Schrade, C. Josephson diode effect in supercurrent interferometers. *Phys. Rev. Lett.* **129**, 267702 (2022).
- [26] Ciaccia, C. *et al.* Gate-tunable Josephson diode in proximitized InAs supercurrent interferometers. *Phys. Rev. Research* **5**, 033131 (2023).
- [27] Casimir, H. B. G. On Onsager's principle of microscopic reversibility. *Rev. Mod. Phys.* **17**, 343–350 (1945).
- [28] Daido, A., Ikeda, Y. & Yanase, Y. Intrinsic superconducting diode effect. *Phys. Rev. Lett.* **128**, 037001 (2022).
- [29] Legg, H. F., Loss, D. & Klinovaja, J. Superconducting diode effect due to magnetochiral anisotropy in topological insulators and Rashba nanowires. *Phys. Rev. B* **106**, 104501 (2022).
- [30] Dartiailh, M. C. *et al.* Phase signature of topological transition in Josephson junctions. *Phys. Rev. Lett.* **126**, 036802 (2021).
- [31] Casparis, L. *et al.* Superconducting gatemon qubit based on a proximitized two-dimensional electron gas. *Nat. Nanotechnol.* **13**, 915–919 (2018).
- [32] Knap, W. *et al.* Weak antilocalization and spin precession in quantum wells. *Phys. Rev. B* **53**, 3912–3924 (1996).
- [33] De Gennes, P. G. *Superconductivity of Metals and Alloys* (Addison–Wesley, 1989).

- [34] Scharf, B., Pientka, F., Ren, H., Yacoby, A. & Hankiewicz, E. M. Tuning topological superconductivity in phase-controlled Josephson junctions with Rashba and Dresselhaus spin-orbit coupling. *Phys. Rev. B* **99**, 214503 (2019).
- [35] Beenakker, C. W. J. Universal limit of critical-current fluctuations in mesoscopic Josephson junctions. *Phys. Rev. Lett.* **67**, 3836–3839 (1991).

Acknowledgments. J. Suh acknowledges supports from Samsung Foundation(SSTF-BA1801-03) and National Research Foundation(RS-2023-00207732, RS-2024-00352688, 2022M3H3A1064154). S.P. acknowledges the support from the Institute for Basic Science (IBS) in the Republic of Korea through the project IBS-R024-Y4.

Ethics declarations

The authors declare no competing interests.

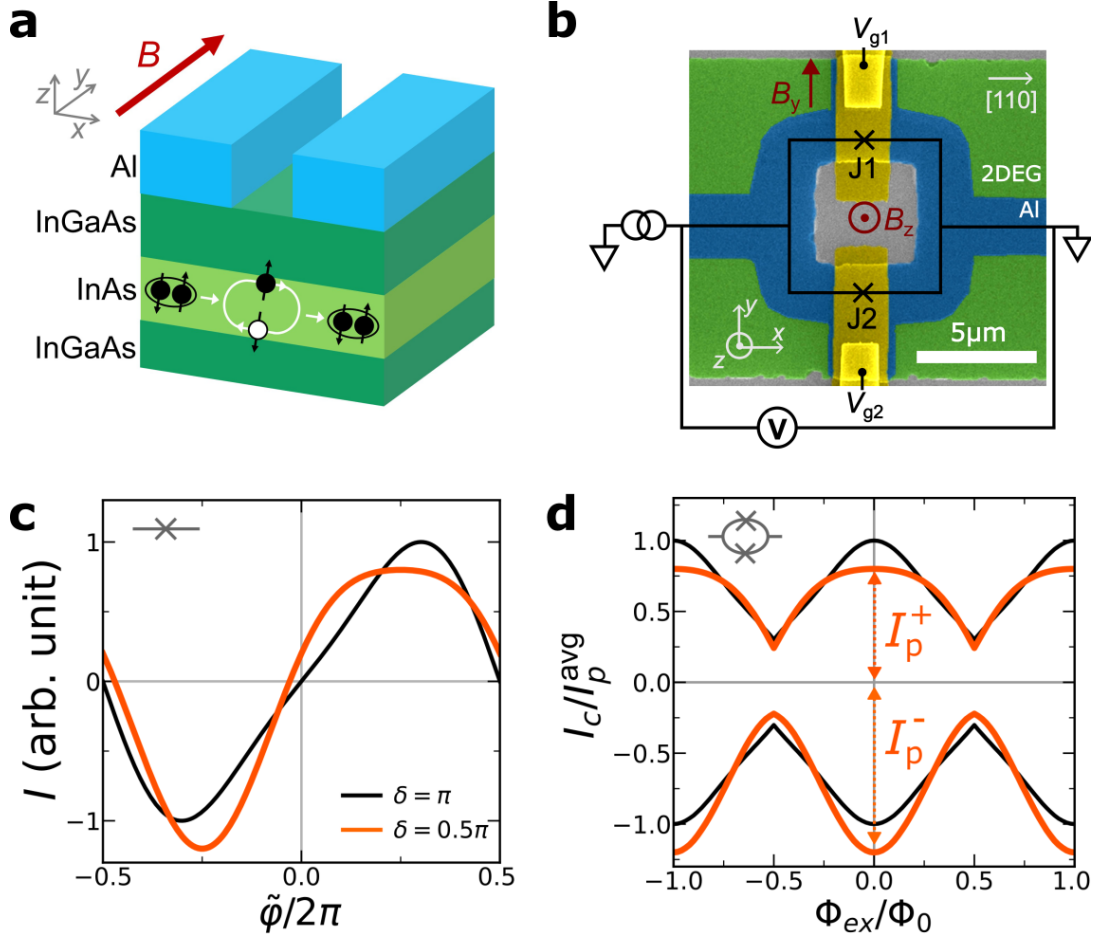


Fig. 1 Al-InAs SQUID and non-reciprocal SQUID oscillation **a**, Schematic representation of a planar SNS JJ based on an Al-InAs heterostructure, with an in-plane magnetic field B_y applied. **b**, False-colored scanning electron microscope (SEM) image and schematic diagram of the SQUID and measurement setup. The white arrow indicates the [110] crystallographic direction of the InAs layer. **c**, $I(\tilde{\varphi})$ of JJs based on Eq. (1). The black solid line corresponds to $\delta = \pi$ and $a_2/a_1 = 0.2$, while the orange solid line is $\delta = \pi/2$ and $a_2/a_1 = 0.2$. **d**, Oscillations of critical current (I_c) in a SQUID consisting of identical JJs, whose CPRs correspond to **c** with the same color codes. Φ_{ex} is the external flux passing through the SQUID loop and Φ_0 is the flux quantum $h/2e$. The oscillations are normalized by the average peak current, $I_p^{\text{avg}} = (I_p^+ + I_p^-)/2$.

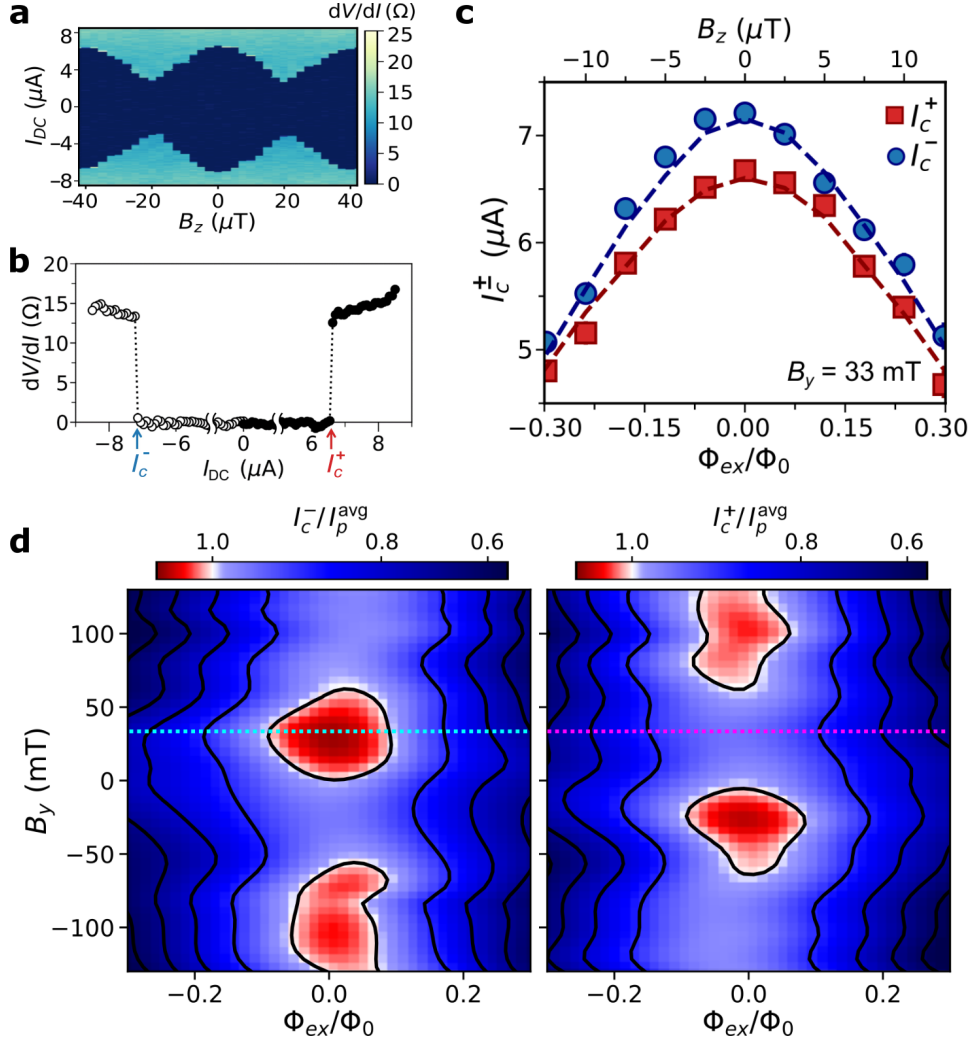


Fig. 2 SQUID oscillation characteristics. **a**, Differential resistance (dV/dI) as a function of I_{DC} and B_z at $V_g = 0$ and $B_y = 33$ mT. **b**, dV/dI as a function of I_{DC} at $B_y = 33$ mT, $B_z = 0$ and $V_g = 0$. The arrows indicate the SQUID critical currents, I_c^- and I_c^+ . **c**, I_c^+ (red squares) and I_c^- (blue circles), near the peak of the SQUID oscillation at $V_g = 0$ and $B_y = 33$ mT. The dashed lines are fit results from a numerically calculated SQUID oscillation. **d**, 2D maps illustrating I_c^- (left panel) and I_c^+ (right panel) as a function of Φ_{ex}/Φ_0 and B_y , normalized by I_p^{avg} for each B_y . The black solid lines indicate contours of constant I_c^-/I_p^{avg} and I_c^+/I_p^{avg} for values 0.6 to 1 in steps of 0.1. The dotted lines mark at $B_y = 33$ mT, as shown in **c**.

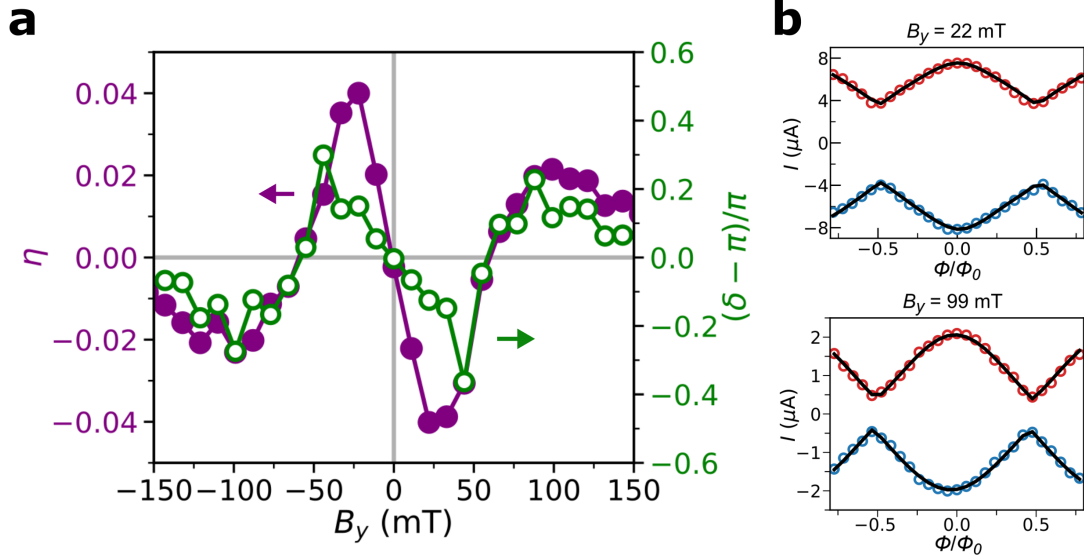


Fig. 3 Josephson diode efficiency and anomalous phase difference. **a**, Josephson diode efficiency (η) and anomalous phase difference (δ) as a function of B_y at $V_g = 0$. **b**, The SQUID oscillation of I_c^+ and I_c^- at $B_y = 22$ and 99 mT. The fits are obtained from Eq. (1). Detailed fitting procedure is shown in Supplementary Information.

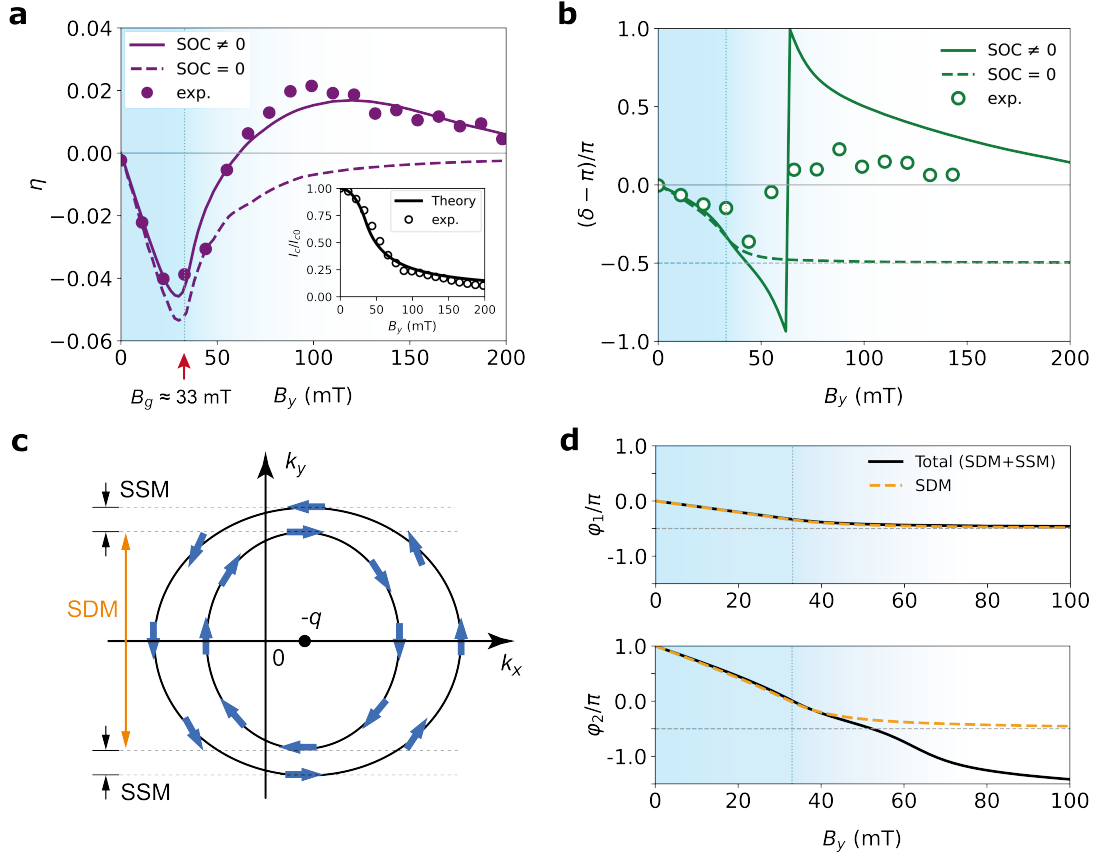


Fig. 4 Calculated diode efficiency and anomalous phase shifts. **a**, The diode efficiency η with and without SOC. The efficiency below $B_g \approx 33$ mT is dominated by fCPM (blue-shaded), and gradually changes to the SOC-assistant regime (white) as the magnetic field increases. That above B_g (white) is affected by the SOC. The B_y dependence of the normalized critical current is shown in the inset. **b**, The anomalous phase difference δ with and without SOC, obtained by fitting the numerical results in **a** with a minimal model for the CPR described in Eq. (1). In **a** and **b**, the data in Fig. 3a are presented together for comparison. **c**, Schematic of the Fermi surfaces with SOC and fCPM. The center shifts by the momentum, $-q$, and the Fermi surfaces are split due to the SOC. The blue arrows denote spin direction with the momentum dependence induced by the SOC. **d**, The first and the second anomalous phase shifts, φ_1 and φ_2 . The phase shifts, illustrated by the black solid lines, correspond to the case of $q \neq 0$ and $\text{SOC} \neq 0$ shown in **a** and **b**. The orange dashed lines depict the phase shifts from SDM only.

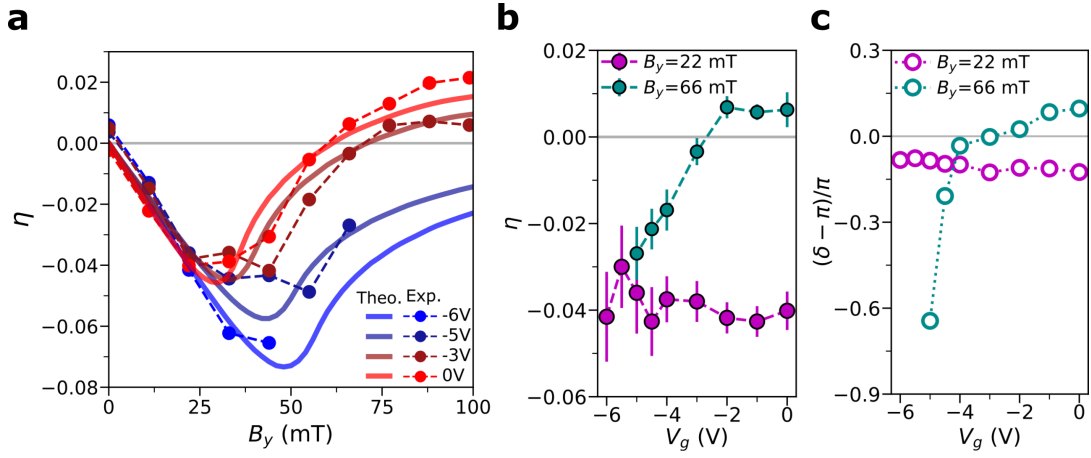


Fig. 5 The electric control of the polarity in JDE. **a**, B_y dependence of the diode efficiency η with varying V_g from -6 V to 0 V. Fitted results using our theoretical model are obtained using parameters summarized in Table 1. **b-c**, The evolution of η and δ with V_g at $B_y = 22$ and 66 mT. In the SOC-assisted regime above $B_y = 55$ mT, the polarity of the JDE is controllable with V_g .

Electric Control of Polarity in Spin-Orbit Josephson Diode

Junghyun Shin¹, Jae-Ho Han^{2,3}, Anjali Rathore⁴, Joon Sue Lee⁴, Seung-Bo Shim⁵,
Jinwoong Cha⁵, Sunghun Park^{3*}, Junho Suh^{1*}

¹Department of Physics, Pohang University of Science and Technology (POSTECH),
Pohang, South Korea.

²Department of Physics, Korea Advanced Institute of Science and Technology (KAIST),
Daejeon, South Korea.

³Center for Theoretical Physics of Complex Systems, Institute of Basic Science, Daejeon,
South Korea.

⁴Department of Physics and Astronomy, University of Tennessee, Knoxville, Tennessee, USA.

⁵Quantum Technology Institute, Korea Research Institute of Standards and Science,
Daejeon, South Korea.

*Corresponding author(s). E-mail(s): sunghun.park@ibs.re.kr, junhosuh@postech.ac.kr;

1 Basic characteristics of Al-InAs heterostructure

To characterize an InAs quantum well (Fig. S1a), we fabricate a top-gated Hall-bar geometry device with the top Al layer removed (Fig. S1b) and measure its transport characteristics. The dependence of density and mobility on gate voltage is presented in Fig. S1c, while Fig. S2c illustrates the gate voltage dependence of Rashba spin-orbit coupling (SOC). Additionally, Fig. S3 displays the superconducting transition temperature and critical magnetic fields of the top Al layer.

An InAs quantum well exhibits two types of SOCs: Rashba and Dresselhaus. Dresselhaus SOC arises due to the lack of inversion symmetry in the crystal structure. In bulk semiconductors with a zinc blende structure, such as GaAs, InAs, and InSb, this broken inversion symmetry naturally leads to cubic Dresselhaus SOC, denoted as γ . In a quantum well, the confinement modifies the electron wave function so that the electron's motion is primarily in the plane of the quantum well. The quantization along the growth direction (z-direction) alters the form of the Dresselhaus SOC, resulting in a linear Dresselhaus SOC, β . Rashba SOC, represented by α , is induced by structural inversion asymmetry, and its strength depends on the net electric field. In a quantum well, an electric field in the z-direction can arise due to the combined effects of structural inversion asymmetry and the mixing of valence band states with conduction band states. This electric field can be further controlled by applying an external electric field through gating.

To examine the evolution of Rashba SOC in the InAs quantum well as a function of gate voltage, we measure a weak antilocalization signal using the Hall-bar device and extract Rashba SOC, α , by analyzing the signal (Fig. S2). We use the theory developed by Iordanski, Lyanda-Geller, and Pikus (ILP) for a 2D electron gas, which is valid when either Rashba SOC or linear Dresselhaus

SOC is dominant [S1, S2].

$$\begin{aligned} \Delta\sigma(B) = & -\frac{e^2}{4\pi^2\hbar} \left\{ \frac{1}{a_0} + \frac{2a_0 + 1 + (H_{SO}/B)}{a_1[a_0 + (H_{SO}/B)] - (2H'_{SO}/B)} \right. \\ & - \sum_{n=1}^{\infty} \left[\frac{3}{n} - \frac{3a_n^2 + 2a_n(H_{SO}/B) - 1 - 2(2n+1)(H'_{SO}/B)}{a_n + (H_{SO}/B)a_{n-1}a_{n+1} - 2(H'_{SO}/B)[(2n+1)a_n - 1]} \right] \\ & \left. + 2 \ln \frac{H_{tr}}{B} + \Psi\left(\frac{1}{2} + \frac{H_\varphi}{B}\right) + 3C \right\} \end{aligned} \quad (\text{S1})$$

$$a_n = n + \frac{1}{2} + \frac{H_\varphi}{B} + \frac{H_{SO}}{B}, \quad H_\varphi = \frac{\hbar}{4el_\phi^2}, \quad H_{tr} = \frac{\hbar}{4eD\tau_e},$$

$$H_{SO} = H_{SO1} + H_{SO3}, \quad H_{SO1} = H_\alpha + H_\beta, \quad H'_{SO} = H_\alpha \text{ or } H_\beta,$$

$$H_{SO3} = \frac{1}{4eD\hbar}(2\Omega_\gamma^2\tau_e), \quad H_\alpha = \frac{1}{4eD\hbar}(2\Omega_\alpha^2\tau_e), \quad H_\beta = \frac{1}{4eD\hbar}(2\Omega_\beta^2\tau_e),$$

$$\Omega_\gamma = \gamma(k_f^3)/4, \quad \Omega_\alpha = \alpha k_f, \quad \Omega_\beta = \beta k_f,$$

where, Ψ is digamma-function, C is Euler's constant, k_f is the Fermi wave vector, and τ_e is the elastic scattering time. In the analysis, we use an effective electron mass of $m^* = 0.023m_e$ and a cubic Dresselhaus SOC value of $\gamma = 2.69 \times 10^{-2} \text{ eV} \cdot \text{nm}^3$, calculated from $\vec{k} \cdot \vec{p}$ theory [S1]. Additionally, we use $\beta = 4.23 \text{ meV} \cdot \text{nm}$, a value employed for fitting the B_y dependence of the diode efficiency (see Extended Data Table 1 in the main text). The estimated β for similar InAs quantum wells in Ref. [S2] is $5 \text{ meV} \cdot \text{nm}$, which is comparable to the value of β we used.

From fitting the weak antilocalization signal, we extract the Rashba SOC, α , and the phase-coherence length, l_ϕ . At $V_g = 0$, the obtained α from the weak antilocalization signal is $8.8 \text{ meV} \cdot \text{nm}$, which is comparable to $\alpha = 7.53 \text{ meV} \cdot \text{nm}$ obtained from fitting the diode efficiency (see Fig. 4a and Extended Data Table 1 in the main text).

The α in the Hall-bar sample is suppressed when a negative gate voltage is applied (Fig. S2c). This is more pronounced than the one obtained from fitting the diode efficiency in the main text. We attribute the discrepancy to the difference in effective gate voltage between the Hall-bar-shaped device with a wide gating region and the superconducting quantum interference device (SQUID) with narrow gating regions.

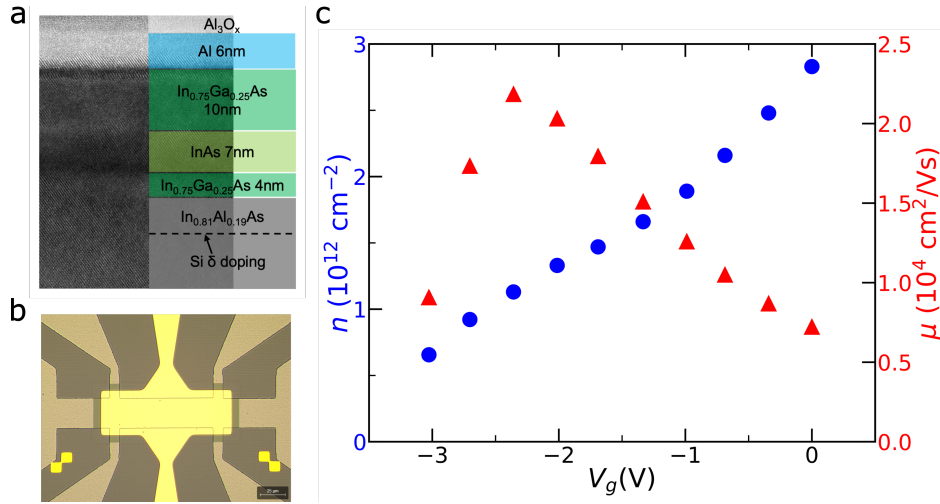


Figure S1 Structure and transport characteristics of an InAs quantum well. **a**, Cross-sectional transmission electron microscopy (TEM) image showing the layered configuration of an Al-InAs heterostructure. **b**, Optical image of a Hall-bar-shaped device with the InAs quantum well with a top gate. **c**, Electron density (n) and mobility (μ) as a function of gate voltage (V_g) in the InAs quantum well.

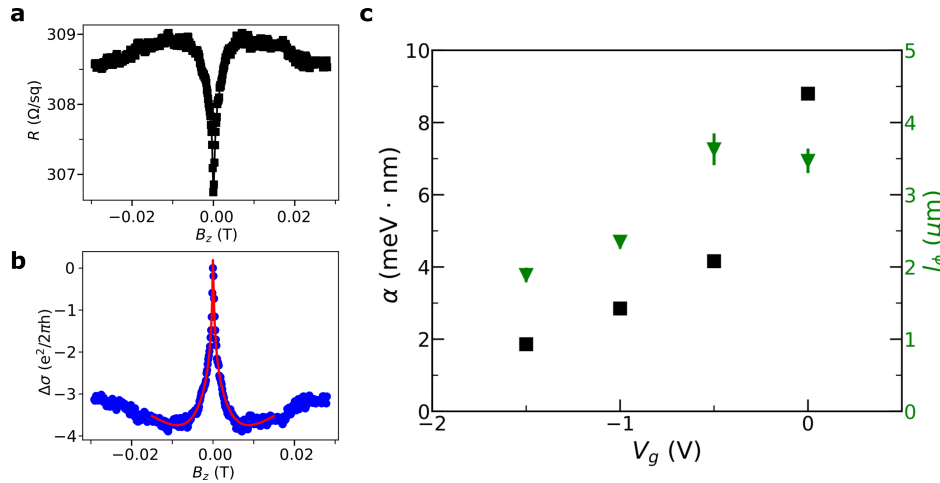


Figure S2 Magnetoconductance analysis and Rashba SOC **a**, Resistance (R) as a function of the perpendicular magnetic fields (B_z) at $V_g = 0$ V. **b**, Magnetoconductance variation ($\Delta\sigma = \sigma(B_z) - \sigma(0)$) plotted as a function of B_z , with blue circles representing the experimental data and the red line indicating the fit using the ILP model. **c**, Rashba SOC α and phase-coherence length l_ϕ as a function of V_g .

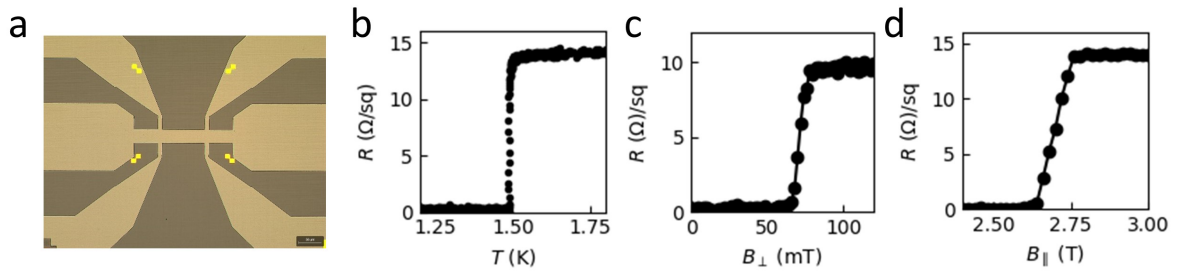


Figure S3 Characteristics of the top superconducting Al layer **a**, Optical image of a Hall-bar-shaped Al film grown on the InAs quantum well. **b**, Resistance (R) as a function of temperature (T) at zero external magnetic field. **c**, R as a function of the out-of-plane magnetic field (B_{\perp}). **d**, R as a function of the in-plane magnetic field (B_{\parallel}).

2 Basic characteristics of Al-InAs SQUID

Figure S4a shows the differential resistance (dV/dI) as a function of B_z (ranging from -0.4 to 0.25 mT) and I_{DC} , measured at $B_y = 0$ and $V_{g1} = V_{g2} = 0$. This figure reveals SQUID oscillations with a period of $4.2E-5$ T, modulated by a Fraunhofer-like pattern in the Josephson junctions (JJs). The oscillation period is approximately half of Φ_0/A_{SQUID} , rather than Φ_0/A_{SQUID} . This is attributed to the larger effective area resulting from magnetic field focusing due to the Meissner effect in the wide SQUID ring [S3].

Figure S4b displays the differential resistance (dV/dI) as a function of B_y and I_{DC} , measured at $B_z = 0$, with $V_{g1} = -15$ V and $V_{g2} = 0$. This gate voltage configuration shows the dependence of the critical current in J2, while J1 is nearly pinched off. The critical current of J2 gradually diminishes with increasing B_y , reaching approximately half its original value near $B_y = 50$ mT. Across the range of 0 to 0.25 T, no nonmonotonic behavior (such as suppression and then revival of the critical current) is observed, which is interpreted as a potential indicator of a topological phase transition [S4].

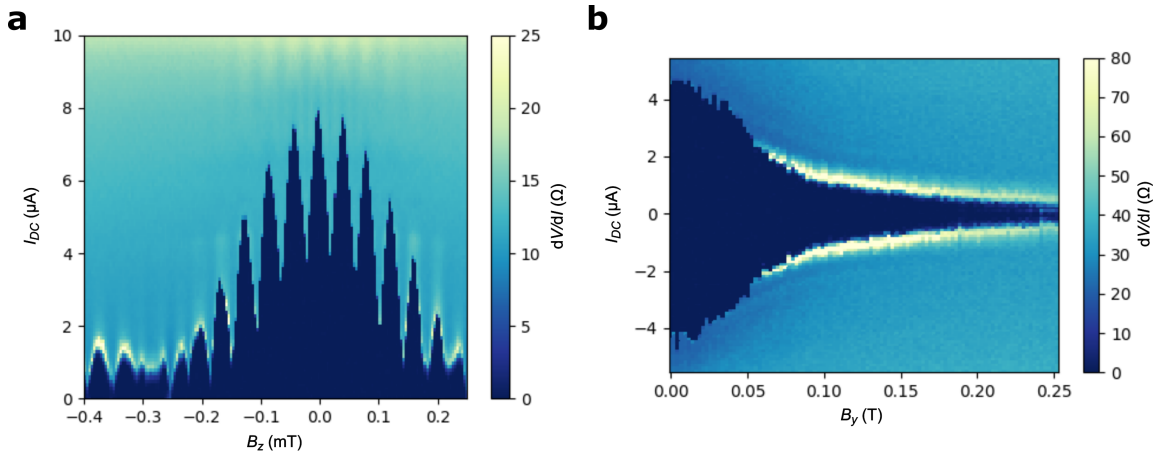


Figure S4 Al-InAs SQUID **a**, Differential resistance (dV/dI) as a function of B_z and I_{DC} at $B_y = 0$ and $V_{g1} = V_{g2} = 0$. **b**, Differential resistance as a function of B_y and I_{DC} at $B_z = 0$, with $V_{g1} = -15$ V and $V_{g2} = 0$.

3 Non-reciprocal critical currents in an Al-InAs SQUID

In SQUIDs, non-reciprocal critical current can arise from having non-identical junctions within the device, even if each junction does not exhibit non-reciprocal properties. In contrast, this study investigates a different source of non-reciprocal critical current: the Josephson diode effect (JDE), where the JJs themselves exhibit non-reciprocal behavior.

We numerically simulate the oscillations of the critical current in a SQUID under two distinct scenarios: one where non-reciprocity arises from junction non-identity and another where it originates from the JDE. These simulations illustrate how the two sources of non-reciprocal critical currents influence a SQUID oscillation differently.

3.1 Critical current oscillations in a SQUID

To calculate the critical current in a SQUID, we consider a DC SQUID composed of two JJs, J1 and J2 (Fig. S5a). We assume the current-phase relations (CPRs) of the JJs include second harmonics, expressed as $I(\varphi) = a_1 \sin(\varphi + \varphi_1) + a_2 \sin(2\varphi + \varphi_2)$, where φ represents the Josephson phase, a_1 and a_2 are the amplitudes of the first and second harmonics, and φ_1 and φ_2 are the phase offsets of the first and second harmonics. This equation can be alternatively expressed as $I(\tilde{\varphi}) = a_1 \sin(\tilde{\varphi}) + a_2 \sin(2\tilde{\varphi} + \delta)$, where $\delta = \varphi_2 - 2\varphi_1$. This form is the same as Eq. 1 in the main text. The ratio a_2/a_1 and the phase difference δ determine the efficiency of the JDE, with δ influencing its polarity. For simplicity, we assume that both JJs have identical non-reciprocal characteristics, characterized by the same δ and a_2/a_1 . Then, the CPRs for J1 and J2 are:

$$I_1(\tilde{\varphi}^{J1}) = a_1 \sin(\tilde{\varphi}^{J1}) + a_2 \sin(2\tilde{\varphi}^{J1} + \delta) \quad (\text{S2})$$

$$I_2(\tilde{\varphi}^{J2}) = r_{JJ} (a_1 \sin(\tilde{\varphi}^{J2}) + a_2 \sin(2\tilde{\varphi}^{J2} + \delta)) \quad (\text{S3})$$

, where the superscripts indicate the corresponding JJs. We introduce the parameter r_{JJ} into the CPR for J2 to account for the difference in magnitudes between the two junctions.

Figure S5a shows a schematic diagram of a SQUID, where I is the total current passing through the SQUID, and J is the circulating current in the SQUID loop. The currents passing through JJs I_1 and I_2 can be expressed as $I_1 = I/2 - J$ and $I_2 = I/2 + J$, respectively. Therefore, I and J follow these relationships:

$$I = I_1 + I_2 \quad (\text{S4})$$

and

$$J = \frac{1}{2} (I_2 - I_1). \quad (\text{S5})$$

Due to fluxoid quantization, the Josephson phases satisfy the following relation:

$$\varphi^{J2} - \varphi^{J1} + (2\pi/\Phi_0) (\Phi_{ex} + LJ) = 2\pi n \quad (\text{S6})$$

, where Φ_{ex} is the external flux, L is the SQUID inductance and n is an integer. Using Eq. S5, this can be rewritten as

$$\varphi^{J2} - \varphi^{J1} + (2\pi/\Phi_0) \left(\Phi_{ex} + \frac{1}{2} L(I_2 - I_1) \right) = 2\pi n. \quad (\text{S7})$$

In the numerical calculation, we set the SQUID inductance to 0.18 nH, which provides the best fit to the experimental data (Sec. 4).

To estimate the critical current of a SQUID, we first find numerous combinations of φ^{J1} and φ^{J2} that satisfy Eq. S7 and compute the corresponding I values using Eq. S4. The maximum I value among these is taken as the forward critical current (I_c^+), and the minimum value is considered the backward critical current (I_c^-).

Before discussing the results of the SQUID oscillation computations, we will examine the phase offset in the first harmonic, φ_1 . When $\varphi_1^{J1} \neq 0$ ($\varphi_1^{J2} \neq 0$), the SQUID oscillation is shifted along the Φ_{ex}/Φ_0 axis by φ_1^{J1} ($-\varphi_1^{J2}$) [S5]. Thus, the SQUID oscillation is shifted by $\varphi_1^{J1} - \varphi_1^{J2}$. We assume $\varphi_1^{J1} = \varphi_1^{J2}$, resulting in no shift in the SQUID oscillation in our computations.

Figure S5c shows an example of the calculation results for the case where no supercurrent rectification effect is present, with $\delta = \pi$ and $r_{JJ} = 1$. When $\delta = \pi$, there is no JDE, as shown in the CPR in Fig. S5b. The parameter $r_{JJ} = 1$ indicates that there is no discrepancy between the CPRs of J1 and J2. In this case, the oscillating critical currents are symmetric about both the Φ_{ex} -axis and the I -axis, resulting in the forward and backward critical currents having the same value for all external flux.

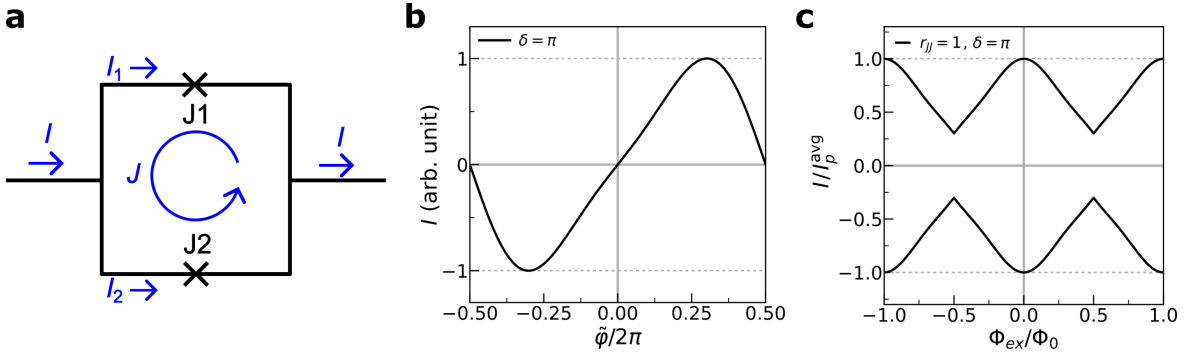


Figure S5 SQUID oscillation **a**, Schematic diagram of a SQUID. **b**, CPR in a JJ with $a_1 = 1$, $a_2/a_1 = 0.2$, and $\delta = \pi$, which corresponds to the black solid line in Fig. 1c of the main text. **c**, Maximum and minimum supercurrent in a SQUID, with $a_1 = 1$, $a_2/a_1 = 0.2$, $\delta = \pi$, and $r_{JJ} = 1$, which corresponds to the black solid line in Fig. 1d of the main text. $I_p^{avg} = (I_p^+ - I_p^-)/2$, where I_p^+ and I_p^- are the maximum magnitudes of the maximum and minimum supercurrent oscillations, respectively.

3.2 Non-reciprocity due to non-identical JJs

We demonstrate the non-reciprocal supercurrent effect due to non-identical JJs in a SQUID, achieved by setting $r_{JJ} \neq 1$. When $r_{JJ} \neq 1$, the critical currents of the two JJs differ, despite all other characteristics being identical. Figure S6 shows examples with $r_{JJ} = 0.5$ and $r_{JJ} = 2$, with the remaining parameters, including δ , are the same as in the SQUID oscillation case shown in Fig. S5c. The SQUID oscillation is no longer symmetric about the Φ_{ex} -axis and the I -axis. This deformation of the SQUID oscillation leads to a non-reciprocal critical current. In Fig. S6c-d, the non-reciprocal diode effect reaches its maximum at $\Phi_{ex}/\Phi_0 = \pm 0.34$ and ± 0.66 . To observe this non-reciprocal supercurrent effect, the device must meet specific conditions, such as having a non-zero SQUID inductance or higher harmonics in the CPR of the JJs[S6–S8].

Despite the asymmetry about the Φ_{ex} -axis and I -axis, the anti-symmetry condition $|I_c^+|(\Phi_{ex}) = -|I_c^-|(-\Phi_{ex})$ remains. This ensures that the maximum magnitudes of the forward and backward critical currents, I_p^+ and I_p^- , are still equal. This behavior differs from the non-reciprocal SQUID oscillations driven by the JDE (Sec.3.3).

We also experimentally demonstrate this non-reciprocal supercurrent effect in our SQUID by applying different values, V_{g1} and V_{g2} , to J1 and J2, respectively, as shown in Fig. S7b with $V_{g1} = -4V$ and $V_{g2} = 0V$. The critical currents of J1 and J2, which are gate-tunable Al-InAs JJs, can be controlled by adjusting V_{g1} and V_{g2} . In this case, $B_y = 0$, where the JDE is absent. The different values of V_{g1} and V_{g2} lead to asymmetry in the critical currents of the two JJs. This difference in critical currents results in non-reciprocal critical currents in the SQUID.

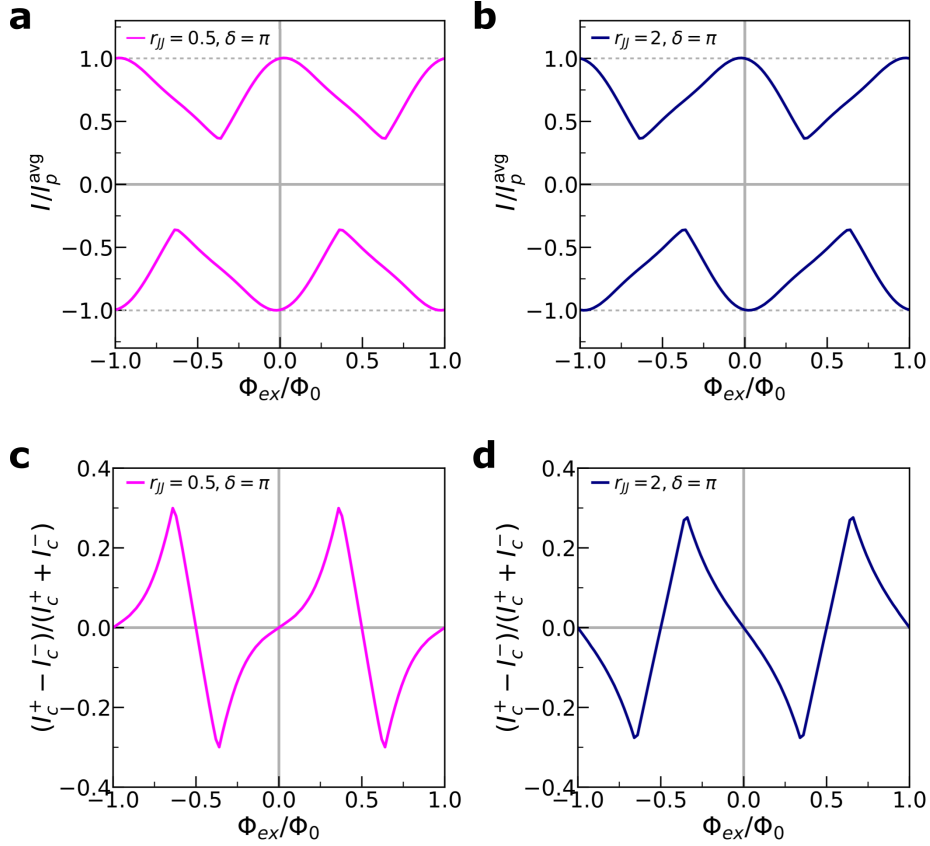


Figure S6 Critical current oscillation of a SQUID with non-identical JJs **a**, Maximum and minimum supercurrent in a SQUID, with $a_1 = 1$, $a_2/a_1 = 0.2$, $\delta = \pi$, and $r_{JJ} = 0.5$. **b**, Maximum and minimum supercurrent in a SQUID, with $a_1 = 1$, $a_2/a_1 = 0.2$, $\delta = \pi$, and $r_{JJ} = 2$. **c**, $(I_c^+ - I_c^-)/(I_c^+ + I_c^-)$ as a function of Φ_{ex}/Φ_0 for the case with $a_1 = 1$, $a_2/a_1 = 0.2$, $\delta = \pi$ and $r_{JJ} = 0.5$. **d**, $(I_c^+ - I_c^-)/(I_c^+ + I_c^-)$ as a function of Φ_{ex}/Φ_0 , for the case with $a_1 = 1$, $a_2/a_1 = 0.2$, $\delta = \pi$, and $r_{JJ} = 2$.

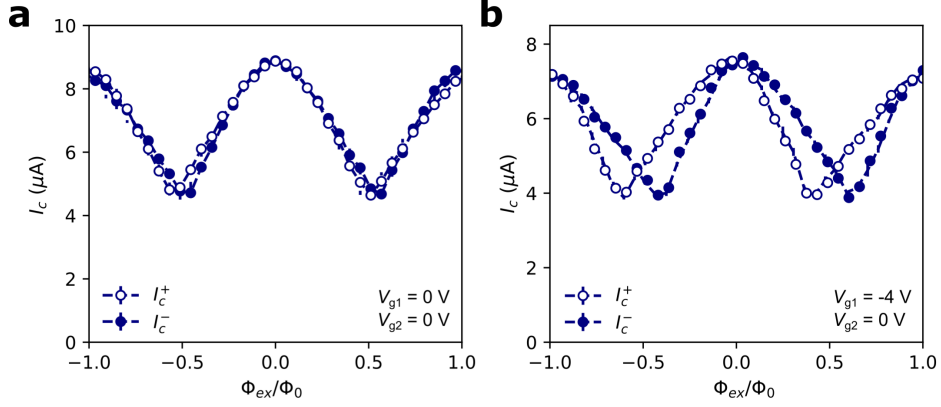


Figure S7 Critical current oscillation of the SQUID with different gate voltage combinations **a**, SQUID oscillation of forward and backward critical currents with $V_{g1} = 0$ V and $V_{g2} = 0$ V. **b**, SQUID oscillation of forward and backward critical currents with $V_{g1} = -4$ V and $V_{g2} = 0$ V.

3.3 Non-reciprocity due to JDE

We demonstrate the distinct non-reciprocal supercurrent effect in a SQUID, which results from the JDE. To induce the JDE in the CPRs of JJs, we set $\delta = \pi/2$ and $3\pi/2$ (Figs. S8a and d). The other parameters, including r_{JJ} , are the same as those in the SQUID oscillation case shown in Fig. S5c. For $\delta = \pi/2$ ($0 < \delta < \pi$), the JDE occurs in the backward current direction, whereas for $\delta = 3\pi/2$ ($\pi < \delta < 2\pi$), it occurs in the forward current direction. The JDE causes the amplitude of the SQUID oscillations to vary with the direction of the current (Fig. S8b and e). Although the SQUID oscillation remains symmetric about the Φ_{ex} -axis, it becomes asymmetric about the I -axis due to the direction-dependent oscillation amplitude. This leads to a non-reciprocal critical current, maximized at the peaks of the SQUID oscillation, I_p^+ and I_p^- .

Figure S9 demonstrates the supercurrent rectification resulting from the JDE. At $B_y = 33$ mT $\Phi_{ex}/\Phi_0 = 0$, and $V_{g1} = V_{g2} = 0$ V, I_p^+ is $6.6 \mu\text{A}$, while I_p^- is $7.25 \mu\text{A}$ (Fig. S9b). Due to the non-reciprocal critical currents, when a current with an amplitude of $7 \mu\text{A}$ is applied, a dissipationless current is observed only in the backward direction, whereas a dissipative current flows in the opposite direction (Fig. S9c).

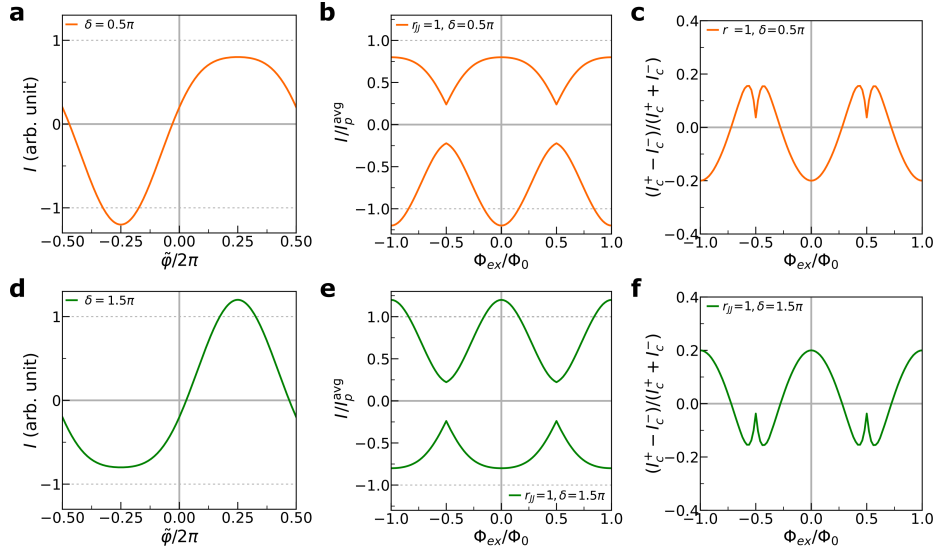


Figure S8 Critical current oscillation of a SQUID with JDE **a**, CPR in a JJ with $a_1 = 1$, $a_2/a_1 = 0.2$, and $\delta = \pi/2$, which corresponds to the orange solid line in Fig. 1c of the main text. **b**, Maximum and minimum supercurrent in a SQUID, with $a_1 = 1$, $a_2/a_1 = 0.2$, $\delta = \pi/2$, and $r_{JJ} = 1$, which corresponds to the orange solid line in Fig. 1d of the main text. **c**, $(I_c^+ - I_c^-)/(I_c^+ + I_c^-)$ as a function of Φ_{ex}/Φ_0 , for the case with $a_1 = 1$, $a_2/a_1 = 0.2$, $\delta = \pi/2$, and $r_{JJ} = 1$. **d**, CPR in a JJ with $a_1 = 1$, $a_2/a_1 = 0.2$, and $\delta = 3\pi/2$. **e**, Maximum and minimum supercurrent in a SQUID, with $a_1 = 1$, $a_2/a_1 = 0.2$, $\delta = 3\pi/2$, and $r_{JJ} = 1$. **f**, $(I_c^+ - I_c^-)/(I_c^+ + I_c^-)$ as a function of Φ_{ex}/Φ_0 , for the case with $a_1 = 1$, $a_2/a_1 = 0.2$, $\delta = 3\pi/2$, and $r_{JJ} = 1$.

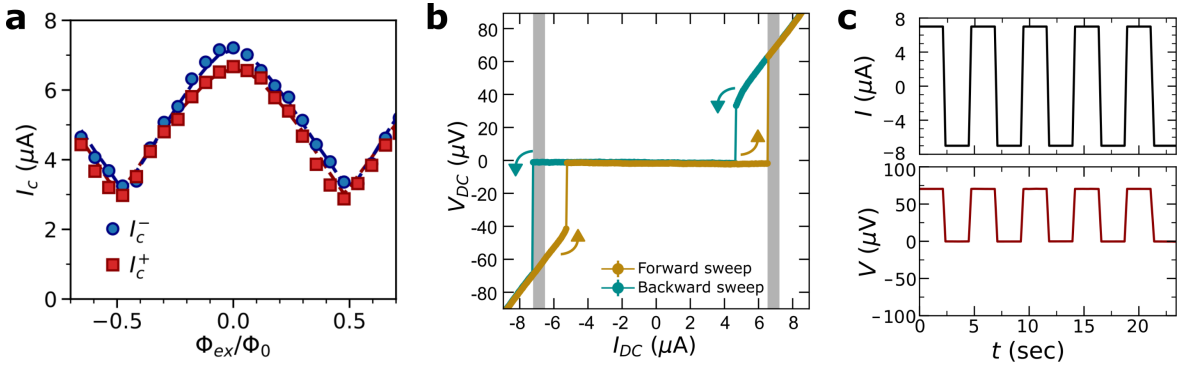


Figure S9 Demonstration of supercurrent rectification due to the JDE **a**, SQUID oscillations of forward and backward critical currents with $B_y = 33$ mT and $V_{g1} = V_{g2} = 0$. **b**, Current-voltage (I - V) characteristics for forward and backward current sweeps at $B_y = 33$ mT, $V_{g1} = V_{g2} = 0$, and $\Phi_{ex}/\Phi_0 = 0$. The gray-shaded region represents the current range between I_c^+ and I_c^- . **c**, Supercurrent rectification demonstrated under the same condition as the I - V characteristics in **b**. The applied current amplitude is $7 \mu\text{A}$, which falls within the gray-shaded range.

4 Extraction of anomalous phase difference δ

We extract the phase difference δ by fitting SQUID oscillations with numerically calculated SQUID oscillations. The fitting process is performed using a Python script, as shown below.

```
# In[1]: List of libraries
import numpy as np
from scipy.optimize import curve_fit
import scipy.constants as const
import math

# In[2]: Define Functions
pi = math.pi
e= const.e
h=const.h
QF = h/(2*e)

#Current phase relation
def CPR_1st(d0,l1,ph1):
    d = d0+ph1
    return l1*np.sin(d)
def CPR_2nd(d0,l1,r_2nd,delta_pi,ph1):
    d = d0+ph1
    delta = delta_pi+pi # delta_pi = delta-pi
    return l1*(r_2nd*np.sin(2*d+delta))
def CPR(d0,l1,r_2nd,delta_pi,ph1):
    return CPR_1st(d0,l1,ph1) + CPR_2nd(d0,l1,r_2nd,delta_pi,ph1)

#Eq. S4
def JJ_e_1(d01,d02,l1,r_2nd,delta_pi,ph1,ph2,r_JJ):
    i = CPR(d01,l1,r_2nd,delta_pi,ph1)+r_JJ*CPR(d02,l1,r_2nd,delta_pi,ph2)
    return i

#Eq. S5
def JJ_e_2(d01,d02,l1,r_2nd,delta_pi,ph1,ph2,r_JJ):
    j = 0.5*(r_JJ*CPR(d02,l1,r_2nd,delta_pi,ph2)-CPR(d01,l1,r_2nd,delta_pi,ph1))
    return j

#Eq. S6
def function(phi_ex,d01,d02,beta_L,lc1,r_2nd,delta_pi,ph1,ph2,r_JJ):
    temp = d02 - d01 + (2*pi/QF)*(phi_ex+L*JJ_e_2(d01,d02,lc1,r_2nd,delta_pi,ph1,ph2,r_JJ))
    return temp

def SQUID(phi_a,lc1,r_2nd,r_JJ,delta_pi,ph2):

    d02 = 2*pi*np.linspace(0, 1, num = 501,endpoint = True)
    d01 = 2*pi*np.linspace(-4, 2, num = 3001,endpoint = True)

    lc = np.zeros(len(phi_a))

    L = 0.18E-9

    ph1 = 2*pi*0

    for k in range(len(phi_a)):
        phi_ex = phi_a[k]
        i = np.zeros(len(d02))
        for n in range(len(d02)):
            d2 = d02[n]
            temp = function(phi_ex,d01,d2,beta_L,lc1,r_2nd,delta_pi,ph1,ph2,r_JJ)
            d1 = d01[np.argmin(np.absolute(temp))]
```

```

i[n] = JJ_e_1(d1,d2,lc1,r_2nd,delta_pi,ph1,ph2,r_JJ)

# a multi-valued function -> a single-valued function
if phi_a[k] > 1:
    lc[k] = np.amin(i);
else:
    lc[k] = np.amax(i);
return lc

# In [3]: Import data
data_p = np.loadtxt('data/Bz_lc_positive_avg_std.txt')
data_n = np.loadtxt('data/Bz_lc_negative_avg_std.txt')

# In [3]: Fit data
X_temp_p = data_p[3:30,0]/4.2E-5
X_temp_n = data_n[3:30,0]/4.2E-5

# a multi-valued function -> a single-valued function
X = np.append(X_temp_p,X_temp_n+2)
Y = np.append((data_p[3:30,1])*1E6,(data_n[3:30,1])*1E6)

p_i = np.array([3.5,0.1,1,0,0])
popt, pcov = curve_fit(SQUID, X, Y, p0 = p_i, bounds=([0.1,0,0.5,-1*pi,-1*pi],
[5,0.3,2,pi,pi]))

```

The critical current in a SQUID is a multi-valued function of Φ_{ex}/Φ_0 with two values depending on the polarity, I_c^+ and I_c^- . To fit a multi-valued function, we use a simple technique. We modify the multi-valued function to a single-valued function by shifting the backward critical currents along the Φ_{ex}/Φ_0 -axis by +2 (Fig. S10b). This modification allows us to fit the multi-valued data and extract the second harmonic parameters in the CPR, particularly δ . When presenting the fit result, the shifted backward critical currents and the fit curve are shifted along the Φ_{ex}/Φ_0 -axis by -2, restoring the modified data to its original form.

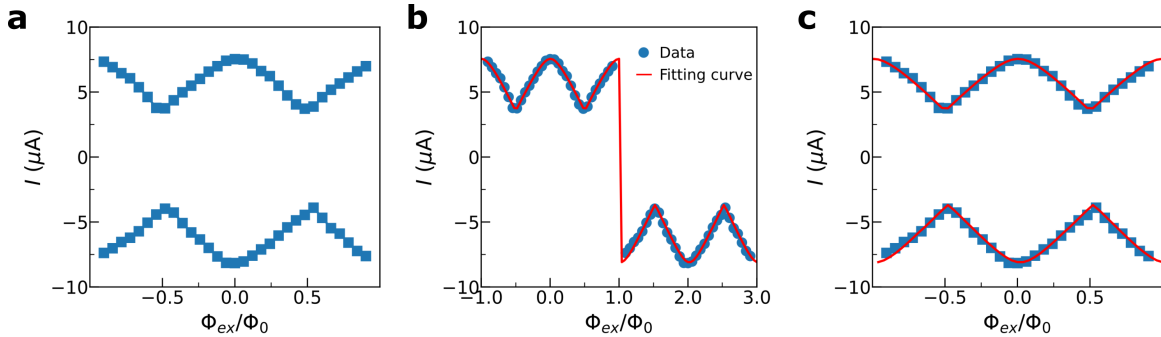


Figure S10 Fitting procedure **a**, The data of the SQUID oscillation of forward and backward critical current. **b**, The fitting result with the modified single-valued SQUID oscillation function. **c**, The final results of the fitting procedure.

5 Spin-orbit coupling and finite Cooper-pair momentum

Our theoretical model accounts for Rashba (α) and Dresselhaus (β) SOCs, the former results from the structural inversion asymmetry along the confinement direction, which is the z -direction in our setup, and the latter originates from the lack of inversion symmetry of the crystal structure. In our InAs/InGaAs two-dimensional electron system, the strength of α is tunable and can be controlled by applying an external gate voltage, but Dresselhaus coupling β is inherent to the crystal structure and depends on crystallographic direction. Here, we adopt the spin-orbit Hamiltonian from Ref. [S9] which corresponds to the current flow along the [110] direction, and α and β are considered as fitting parameters.

The finite momentum q carried by the Cooper pairs due to the orbital effect of the in-plane magnetic field can be obtained from the second Ginzburg-Landau equation of the screening current density [S10, S11],

$$\vec{j} = -\frac{1}{\mu_0\lambda^2} \left(\vec{A} + \frac{\Phi_0}{2\pi} \nabla\varphi \right), \quad (\text{S8})$$

with the permeability μ_0 , the London penetration depth λ , and the superconducting flux quantum $\Phi_0 = h/2e$. The vector potential $\vec{A} = B_y z \hat{x}$ of the magnetic field is set to be zero within the two-dimensional electron gas at $z = 0$. In our Al-InAs heterostructure illustrated in Fig. S11, the superconductor is located at $z = d$ above the electron gas where $d = (d_w + d_s)/2$ is one-half of the total thickness of the semiconducting quantum well (d_w) and the superconductor (d_s). Within the superconducting region $d - d_s/2 < z < d + d_s/2$, we assume that the screening current is uniform in the y -direction and it flows in the x -direction in opposite direction on the different sides with respect to $z = d$ at which the current is zero $j_x = 0$ if the self-field generated by the screening current is assumed to be negligible. Using the vector potential approximately given by $\vec{A} = B_y d \hat{x}$ at $z = d$ due to the thin film geometry, we obtain the phase of the superconducting order parameter,

$$\varphi = 2qx + \text{const.}, \quad q = -\frac{\pi B_y d}{\Phi_0}, \quad (\text{S9})$$

where the const. is the integration constant. Without loss of generality, we absorb the constant into φ_0 . Note that the sign of q is reversed if we switch the coordinate frame from right-handed to left-handed [S11].

In general, fCPM q_{soc} may be induced by strong Rashba SOC with the magnetic field. In experiments, one can distinguish this spin-orbit-induced Cooper pair momentum from that due to the orbital effect by measuring the gate-voltage dependence of the supercurrent diode effect as the strength of the Rashba coupling is varied by the gate voltage. In our experiments, the gate-voltage dependence is very weak at low magnetic field, indicating that the Cooper pair momentum is due to the orbital effect. With the parameters of $\alpha = 10$ meV nm and $v_F = 5.1 \times 10^5$ m/s used in our theoretical calculation, we estimate the value of q_{soc} [S12],

$$|q_{\text{soc}}| = \left| \alpha \frac{1}{\hbar^2 v_F^2} \frac{g\mu_B B_y}{2} \right| \approx 4.41 \times 10^{-8} B_y \text{ mT}^{-1} \text{ nm}^{-1}, \quad (\text{S10})$$

which is three orders of magnitude smaller than the orbital-induced momentum $q \approx 1.5 \times 10^{-5} B_y \text{ mT}^{-1} \text{ nm}^{-1}$. Therefore, we neglected this effect in the calculation.

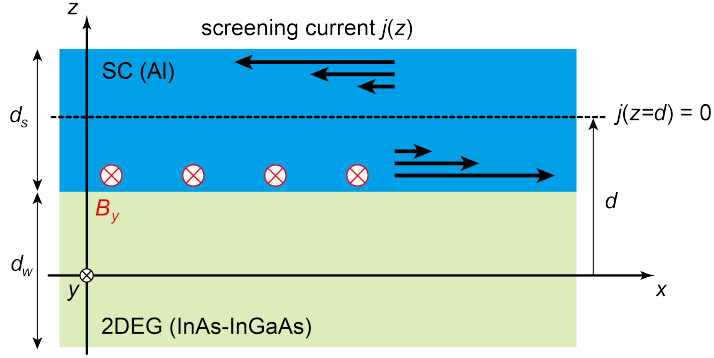


Figure S11 Schematic figure showing orbital induced fCPM. External magnetic field B_y is screened within the bulk SC by generating a screening current near the surfaces. The screening current induces finite momentum to the Cooper pairs in two-dimensional electron gas (2DEG) by proximity effects.

6 Scattering matrices of the Josephson junction

In this section, we provide the details of the calculation of the CPR through scattering formalism in a single JJ. The Bogoliubov-de Gennes (BdG) equation for the JJ is

$$H_{\text{BdG}}\Psi = E\Psi, \quad H_{\text{BdG}} = \begin{pmatrix} H_0 - \mu & \Delta(x) \\ \Delta^*(x) & -\mathcal{T}H_0\mathcal{T}^{-1} + \mu \end{pmatrix}, \quad (\text{S11})$$

where $\Psi = (\psi_{e\uparrow}, \psi_{e\downarrow}, \psi_{h\downarrow}, -\psi_{h\uparrow})^T$ is the Nambu spinor, E is the excitation energy, H_0 is the normal state Hamiltonian, μ is the chemical potential measured from the bottom of the electron band. $\mathcal{T} = -i\sigma_y\mathcal{C}$ is the time-reversal operator with Pauli matrices σ_i ($i = x, y, z$) and complex conjugation \mathcal{C} , and $\Delta(x)$ is the pairing potential varying along the junction direction x . The form of $\Delta(x)$ is given by

$$\Delta(x) = \Delta e^{i2qx} [\Theta(-x) + e^{i\varphi}\Theta(x - L_j)], \quad (\text{S12})$$

where q is orbital-induced fCPM discussed in Sec. 5, $\Delta = 170 \mu\text{eV}$ is the proximity-induced gap, φ is the superconducting phase difference, L_j is the length of the junction, and $\Theta(x)$ is the step function. For the normal state Hamiltonian H_0 , we use a two-dimensional electron gas model with SOC under the applied magnetic field along the y -direction:

$$H_0(k_x, k_y) = \frac{\hbar^2(k_x^2 + k_y^2)}{2m^*} - (\alpha + \beta)k_x\sigma_y + (\alpha - \beta)k_y\sigma_x + (V_b + E_Z\sigma_y)L_j\delta(x). \quad (\text{S13})$$

Here, $m^* = 0.023m_e$ is the effective mass, α is the Rashba SOC constant, and β is the Dresselhaus SOC constant along [110] crystallographic direction. V_b represents potential scattering strength, $E_Z = g\mu_B B_y/2$ is the Zeeman energy with g -factor $g = -17$. We assume that E_Z and V_b are present only at the junction region $0 < x < L_j$ and zero elsewhere. The width of the junction $W = 4 \mu\text{m}$ is much larger than $L_j = 100 \text{ nm}$.

We consider a short junction limit $L_j \ll \xi = \hbar v_F/\Delta$. For $\mu = 17 \text{ meV}$, the superconducting coherence length is $\xi = 2 \mu\text{m}$, and the short junction condition is well satisfied. Therefore, we approximate the scattering processes occurring at $x = 0$, as shown in the last term in Eq. (S13).

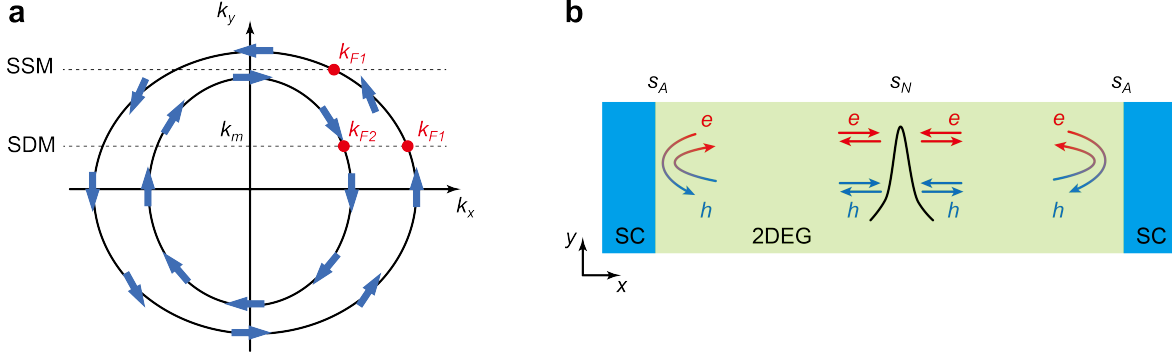


Figure S12 a, Two spin-split Fermi surfaces due to SOCs. The spin direction (blue arrow) is locked at each Fermi momentum. Spin-split modes (SSM) and spin-degenerate modes (SDM) have one (k_{F1}) and two fermi points (k_{F1} and k_{F2}), respectively. **b**, Schematic figure for the scatterings occurring in the Josephson junction. The normal scattering (s_N) scatters electrons (holes) to electrons (holes), while the Andreev reflections occurring at the superconducting-normal metal interfaces convert electrons (holes) to holes (electrons).

In addition, we focus on the regime where the chemical potential is much larger than the superconducting gap, $\mu \gg \Delta$, allowing us to neglect the normal reflection at the interface between the superconductor and the normal region can be neglected (Andreev approximation).

The problem can be reduced to quasi-one-dimensional problem with multiple transverse modes. Imposing hard-wall boundary conditions at $y = 0$ and W on $\Psi(x)$, the wave vector k_y becomes quantized as $k_m = m\pi/W$, where $m \in \mathbb{Z}$. The physical confinement along the y -direction results in multiple transverse subbands labeled by m . The choice of boundary conditions would be irrelevant in our case of $W \gg L_j$. Then, the normal state Hamiltonian for given transverse mode m is,

$$H_0(k_x; m) = \frac{\hbar^2(k_x^2 + k_m^2)}{2m^*} - (\alpha + \beta)k_x\sigma_y + (\alpha - \beta)k_m\sigma_x + (V_b + E_Z\sigma_y)L_j\delta(x). \quad (\text{S14})$$

The number of bands of the effective one-dimensional Hamiltonian $H_0(k_x; m)$ can be one or two depending on the value of m , originating from the spin-split two-dimensional bands of $H_0(k_x, k_y)$ by the SOCs. We refer to the modes with single-band with $k_{y2} < |k_m| < k_{y1}$ and double-band $|k_m| < k_{y2}$ as spin-split mode (SSM) and spin-degenerate mode (SDM), respectively (Fig. S12a). Here,

$$k_{y1} = \sqrt{k_F^2 + \frac{1}{4}(\tilde{\alpha} - \tilde{\beta})^2} + \frac{|\tilde{\alpha} - \tilde{\beta}|}{2}, \quad k_{y2} = \sqrt{k_F^2 + \frac{1}{4}(\tilde{\alpha} - \tilde{\beta})^2} - \frac{|\tilde{\alpha} - \tilde{\beta}|}{2}, \quad (\text{S15})$$

with $k_F = \sqrt{2m^*\mu}/\hbar$, $\tilde{\alpha} = 2m^*\alpha/\hbar^2$, and $\tilde{\beta} = 2m^*\beta/\hbar^2$. For convenience, we provide the eigenvalues and eigenstates of $H_0(k_x; m) - \mu$:

$$\epsilon_{\pm}(k_x) = \frac{\hbar^2(k_x^2 + k_m^2)}{2m^*} - \mu \pm \sqrt{\alpha_+^2 k_x^2 + \alpha_-^2 k_m^2}, \quad \chi_{\pm}(k_x) = \frac{1}{\sqrt{2}} \begin{pmatrix} 1 \\ \mp e^{i\theta_{\text{soc}}} \end{pmatrix}, \quad (\text{S16})$$

where $\alpha_{\pm} = \alpha \pm \beta$ and

$$e^{i\theta_{\text{soc}}} = \frac{i\alpha_+ k_x - \alpha_- k_m}{\sqrt{\alpha_+^2 k_x^2 + \alpha_-^2 k_m^2}}. \quad (\text{S17})$$

Below, we provide the scattering matrices $s_N^{(m)}$ and $s_A^{(m)}$ in detail. We will drop the mode index m for convenience unless indicated otherwise.

6.1 Spin-split mode (SSM)

There are two Fermi points at $k_x = \pm k_{F_1}$ from which $\epsilon_-(k_x) = 0$,

$$k_{F_1} = \sqrt{k_F^2 - k_m^2 + \frac{(\tilde{\alpha} + \tilde{\beta})^2}{2} + \sqrt{(\tilde{\alpha} + \tilde{\beta})^2 k_F^2 + \frac{(\tilde{\alpha} + \tilde{\beta})^4}{4} - 4\tilde{\alpha}\tilde{\beta}k_m^2}}. \quad (\text{S18})$$

Only the modes near the Fermi points are relevant in a low-energy limit. Then, one can write the electron wave function $\psi_e(x)$ as a linear combination of the left- and right-moving states,

$$\psi_e(x) = e^{ik_{F_1}x} \chi_R \psi_{eR}(x) + e^{-ik_{F_1}x} \chi_L \psi_{eL}(x), \quad (\text{S19})$$

where $\chi_R = \chi_-(k_{F_1})$ and $\chi_L = \chi_-(-k_{F_1})$ are the right-moving and left-moving eigenstates of $H_0(k_x; m) - \mu$ at $k_x = \pm k_{F_1}$, respectively. Neglecting the rapidly oscillating modes ($\sim e^{\pm 2ik_{F_1}x}$), we obtain

$$\tilde{H}_0 - \mu = \begin{pmatrix} \hbar v_{F_1}(k_x - k_{F_1}) & 0 \\ 0 & -\hbar v_{F_1}(k_x + k_{F_1}) \end{pmatrix}, \quad v_{F_1} = \left. \frac{1}{\hbar} \frac{\partial \epsilon_-(k_x)}{\partial k_x} \right|_{k_x=k_{F_1}}. \quad (\text{S20})$$

We will neglect the $-\hbar v_{F_1} k_{F_1}$ term in the Hamiltonian henceforth for simplicity, as it does not affect the scattering matrices. Note that the spin degree of freedom is locked, so \tilde{H}_0 is still 2×2 matrix. The same procedure for the hole part yields the linearized Hamiltonian for the basis $\tilde{\Psi} = (\psi_{eR}, \psi_{eL}, \psi_{hR}, \psi_{hL})^T$,

$$\tilde{H}_{\text{BdG}} \tilde{\Psi} = E \tilde{\Psi}, \quad \tilde{H}_{\text{BdG}} = \begin{pmatrix} -i\hbar v_{F_1} \hat{d}_z \partial_x & \Delta(x) \\ \Delta^*(x) & i\hbar v_{F_1} \hat{d}_z \partial_x \end{pmatrix} + \begin{pmatrix} \hat{V} + \hat{Z} & 0 \\ 0 & -\hat{V} + \hat{Z} \end{pmatrix} \delta(x), \quad (\text{S21})$$

where \hat{d}_i ($i = x, y, z$) is Pauli matrices in the right/left mover space. The pairing potential $\Delta(x)$ is diagonal in the right-left mover space because of the electron-hole symmetry. The barrier terms \hat{V} and \hat{Z} are written as

$$\hat{V} = \begin{pmatrix} \langle \chi_R | V_b L_j | \chi_R \rangle & \langle \chi_R | V_b L_j | \chi_L \rangle \\ \langle \chi_L | V_b L_j | \chi_R \rangle & \langle \chi_L | V_b L_j | \chi_L \rangle \end{pmatrix}, \quad (\text{S22})$$

$$\hat{Z} = \begin{pmatrix} \langle \chi_R | E_z \sigma_y L_j | \chi_R \rangle & \langle \chi_R | E_z \sigma_y L_j | \chi_L \rangle \\ \langle \chi_L | E_z \sigma_y L_j | \chi_R \rangle & \langle \chi_L | E_z \sigma_y L_j | \chi_L \rangle \end{pmatrix}. \quad (\text{S23})$$

With Pauli matrices $\hat{\tau}_i$ ($i = x, y, z$) acting on the particle-hole space, we perform a unitary transformation by $\hat{U} = \exp(-i\frac{\varphi}{2}\Theta(x)\hat{\tau}_z - iq\hat{x}\hat{\tau}_z)$, resulting in

$$H_{\text{SSM}} \Psi_{\text{SSM}} = E \Psi_{\text{SSM}}, \quad H_{\text{SSM}} \equiv \hat{U} \tilde{H}_{\text{BdG}} \hat{U}^\dagger = H_{\text{kin}} + H_b \delta(x) + H_{sc}, \quad (\text{S24})$$

where

$$H_{\text{kin}} = -i\hbar v_{F_1} \hat{d}_z \hat{\tau}_z \partial_x + \hbar v_{F_1} q \hat{d}_z,$$

$$\begin{aligned}
H_b &= \hat{V}\hat{\tau}_z + \hat{Z} + \frac{\hbar v_{F_1}\varphi}{2}\hat{d}_z, \\
H_{sc} &= \Delta[\Theta(-x) + \Theta(x - L_j)].
\end{aligned}$$

The boundary condition of the states across the scatterer at $x = 0$ is then imposed as

$$\Psi_{\text{SSM}}(0^+) = \exp\left(-\frac{i}{\hbar v_{F_1}}\hat{d}_z\hat{\tau}_z H_b\right)\Psi_{\text{SSM}}(-0^+), \quad (\text{S25})$$

where 0^+ is the positive infinitesimal. We convert this transfer matrix to scattering matrix s_N which connects the incoming and outgoing states with respect to $x = 0$ (Fig. S12b),

$$\Psi_{\text{out}} = s_N \Psi_{\text{in}}, \quad (\text{S26})$$

$$\Psi_{\text{in}}(x) = \begin{pmatrix} \psi_{eR}(x) \\ 0 \\ 0 \\ \psi_{hL}(x) \end{pmatrix} \Theta(-x) + \begin{pmatrix} 0 \\ \psi_{eL}(x) \\ \psi_{hR}(x) \\ 0 \end{pmatrix} \Theta(x), \quad (\text{S27})$$

$$\Psi_{\text{out}}(x) = \begin{pmatrix} 0 \\ \psi_{eL}(x) \\ \psi_{hR}(x) \\ 0 \end{pmatrix} \Theta(-x) + \begin{pmatrix} \psi_{eR}(x) \\ 0 \\ 0 \\ \psi_{hL}(x) \end{pmatrix} \Theta(x). \quad (\text{S28})$$

The matrix s_N is given by

$$s_N = \begin{pmatrix} s_0 & 0 \\ 0 & s_0^* \end{pmatrix}, \quad s_0 = \begin{pmatrix} r & e^{i\frac{\varphi}{2}}t' \\ e^{-i\frac{\varphi}{2}}t & r' \end{pmatrix}. \quad (\text{S29})$$

The reflection and transmission coefficients are determined by

$$\begin{aligned}
te^{i\theta_z} &= t'e^{-i\theta_z} = (\cos d + in_z \sin d)^{-1}, \\
re^{-i\theta_{\text{soc}}} &= r'e^{i\theta_{\text{soc}}} = -in_z \sqrt{tt'} \cos \theta_{\text{soc}} \sin d, \\
\theta_z &= \frac{E_z L_j \sin \theta_{\text{soc}}}{\hbar v_{F_1}}, \quad d = \left| \frac{V_b L_j \sin \theta_{\text{soc}}}{\hbar v_{F_1}} \right|,
\end{aligned} \quad (\text{S30})$$

where $n_z = |\sin \theta_{\text{soc}}|^{-1}$ and θ_{soc} is defined in Eq. (S17). The Andreev scattering matrix s_A defined by $\Psi_{\text{in}}^A = s_A \Psi_{\text{out}}^A$ can also be obtained by matching the states at the SN interfaces $|x| = L_j/2$ (Fig. S12b),

$$s_A = \begin{pmatrix} 0 & s_{eh} \\ s_{he} & 0 \end{pmatrix}, \quad s_{eh} = \hat{d}_x s_{he} \hat{d}_x = \begin{pmatrix} \beta_- & 0 \\ 0 & \beta_+ \end{pmatrix}, \quad (\text{S31})$$

with

$$\beta_{\pm} = \frac{E \pm \hbar v_{F_1} q}{\Delta} - i \sqrt{1 - \frac{(E \pm \hbar v_{F_1} q)^2}{\Delta^2}}. \quad (\text{S32})$$

6.2 Spin-degenerate mode (SDM)

For SDMs with double bands, two additional Fermi points at $k_x = \pm k_{F_2}$, where $\epsilon_+(k_x) = 0$, appear on the inner Fermi surface,

$$k_{F_2} = \sqrt{k_F^2 - k_m^2 + \frac{(\tilde{\alpha} + \tilde{\beta})^2}{2}} - \sqrt{(\tilde{\alpha} + \tilde{\beta})^2 k_F^2 + \frac{(\tilde{\alpha} + \tilde{\beta})^4}{4} - 4\tilde{\alpha}\tilde{\beta}k_m^2}. \quad (\text{S33})$$

Following the same procedure as for SSMs, we linearize the Hamiltonian and perform the unitary transformation. In the basis $\Psi_{\text{SDM}} = (\psi_{eR_1}, \psi_{eR_2}, \psi_{eL_1}, \psi_{eL_2}, \psi_{hR_1}, \psi_{hR_2}, \psi_{hL_1}, \psi_{hL_2})^T$, the 8×8 scattering matrices s_N and s_A are obtained. The scattering matrix of electron, s_0 in Eq. (S29), has the form

$$s_0 = \begin{pmatrix} \hat{r} & e^{i\frac{\varphi}{2}} \hat{t}' \\ e^{-i\frac{\varphi}{2}} \hat{t} & \hat{r}' \end{pmatrix}, \quad (\text{S34})$$

where \hat{r} and \hat{r}' (\hat{t} and \hat{t}') are the 2×2 reflection (transmission) matrices describing the scattering between the outer band and the inner band. The matrices s_{eh} and s_{he} of the Andreev scattering matrix s_A in Eq. (S31) are obtained by

$$s_{eh} = \hat{a}_x s_{he} \hat{a}_x = \begin{pmatrix} \hat{\beta}_- & 0 \\ 0 & \hat{\beta}_+ \end{pmatrix}, \quad \hat{\beta}_{\mp} = \begin{pmatrix} \beta_{\mp 1} & 0 \\ 0 & \beta_{\mp 2} \end{pmatrix}, \quad (\text{S35})$$

where $\beta_{\mp j}$ with $j = 1, 2$ are given by

$$\beta_{\mp j} = \frac{E \mp \hbar v_{F_j} q}{\Delta} - i \sqrt{1 - \left(\frac{E \mp \hbar v_{F_j} q}{\Delta} \right)^2}. \quad (\text{S36})$$

7 Evolution of the higher harmonics with magnetic field

We analyze the evolution of the CPR under the magnetic field B_y . The CPRs we discuss here correspond to the case of $q \neq 0$ and $\text{SOC} \neq 0$ presented in Fig. 4 in the main text. The results are shown in Fig. S13.

The plots **a** and **b** in Fig. S13 illustrate how the CPRs evolve with the magnetic field B_y . The CPRs for SDM and SSM show distinct characteristics, such that while $I^{\text{SDM}}(\varphi)$ exhibits the evolution similar to that driven by the fCPM without SOC [S13], $I^{\text{SSM}}(\varphi)$ is shifted with B_y , reflecting the Zeeman effect on the spin-split states. The plots **c** and **d** provide further analysis by showing the amplitudes of the first and the second harmonics obtained from fitting the CPRs with the model in Eq. (1). Note that the amplitudes of the second harmonics, a_2^{SDM} and a_2^{SSM} , in **d** are comparable, demonstrating a strong dependence of the anomalous phase shift of the second harmonic on B_y , as shown in **f**. Such dependence can be seen the following relations,

$$a_2^{\text{SDM}} \sin(2\varphi + \varphi_2^{\text{SDM}}) + a_2^{\text{SSM}} \sin(2\varphi + \varphi_2^{\text{SSM}}) = a_2^{\text{TOTAL}} \sin(2\varphi + \varphi_2^{\text{TOTAL}}),$$

$$\varphi_2^{\text{TOTAL}} = \arctan \left(\frac{a_2^{\text{SDM}} \sin \varphi_2^{\text{SDM}} + a_2^{\text{SSM}} \sin \varphi_2^{\text{SSM}}}{a_2^{\text{SDM}} \cos \varphi_2^{\text{SDM}} + a_2^{\text{SSM}} \cos \varphi_2^{\text{SSM}}} \right). \quad (\text{S37})$$

Therefore, this pronounced variation is attributed to the comparable amplitudes shown in **d**.

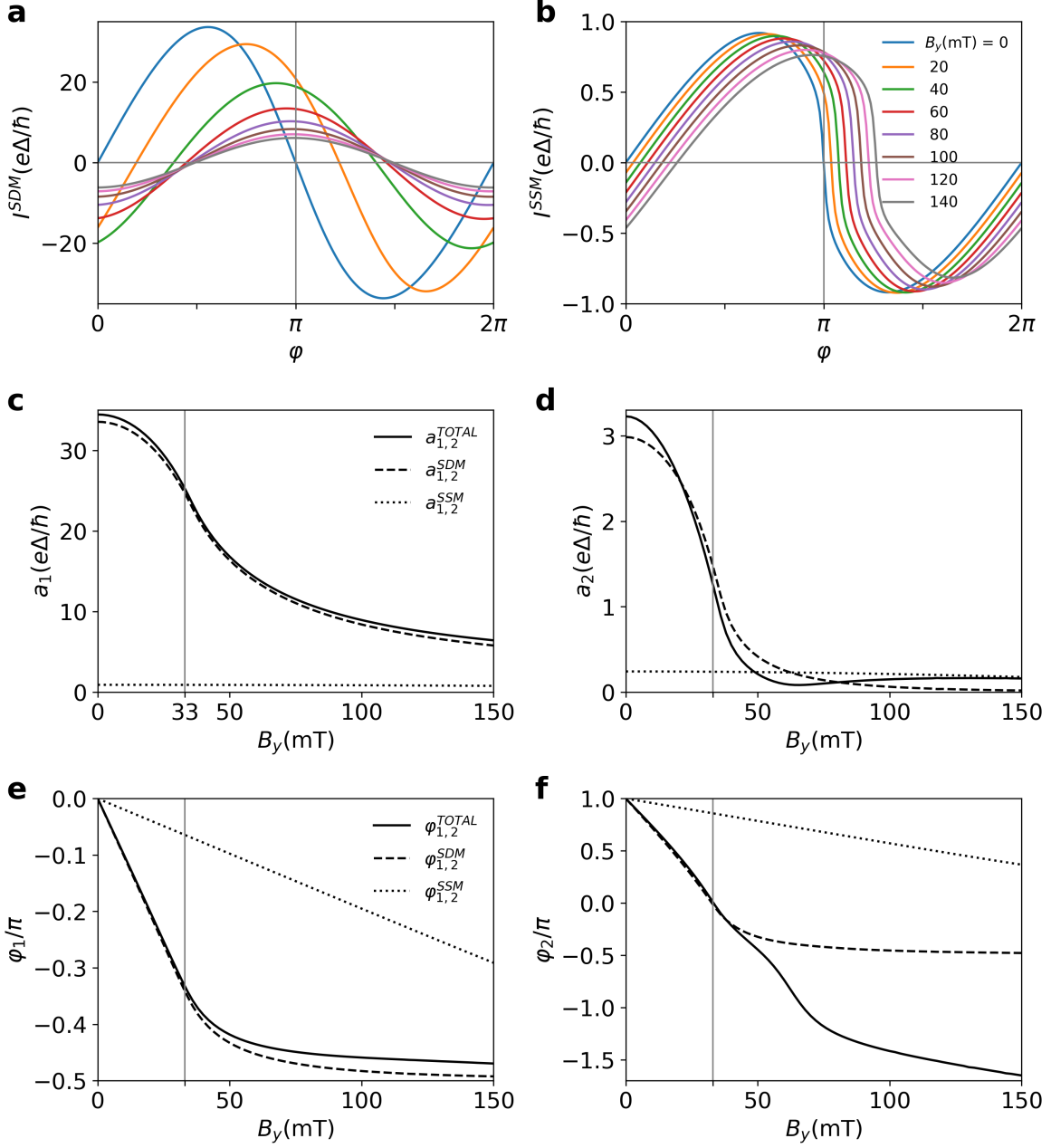


Figure S13 Evolution of the CPR with B_y . **a**, The evolution of the CPR for SDM. **b**, The same as **a**, but for SSM. **c**, Amplitudes of the first harmonic obtained by fitting the CPRs in **a** and **b** to Eq. (1). **d**, Amplitudes of the second harmonic obtained as in **c**. **e**, Anomalous phase shift of the first harmonic obtained as in **c**. **f**, Anomalous phase shift of the second harmonic obtained as in **c**.

References

- [S1] Knap, W. *et al.* Weak antilocalization and spin precession in quantum wells. *Phys. Rev. B* **53**, 3912–3924 (1996).
- [S2] Shabani, J. *et al.* Two-dimensional epitaxial superconductor-semiconductor heterostructures: A platform for topological superconducting networks. *Phys. Rev. B* **93**, 155402 (2016).
- [S3] Brandt, E. H. & Clem, J. R. Superconducting thin rings with finite penetration depth. *Phys. Rev. B* **69**, 184509 (2004).
- [S4] Dartiailh, M. C. *et al.* Phase signature of topological transition in Josephson junctions. *Phys. Rev. Lett.* **126**, 036802 (2021).
- [S5] Mayer, W. *et al.* Gate controlled anomalous phase shift in al/InAs josephson junctions. *Nat. Commun.* **11**, 212 (2020).
- [S6] Clarke, J. & Braginski, A. I. *The SQUID Handbook: Fundamentals and Technology of SQUIDS and SQUID Systems* Vol. 1 (Wiley-VCH, 2004).
- [S7] Souto, R. S., Leijnse, M. & Schrade, C. Josephson diode effect in supercurrent interferometers. *Phys. Rev. Lett.* **129**, 267702 (2022).
- [S8] Ciaccia, C. *et al.* Gate-tunable josephson diode in proximitized InAs supercurrent interferometers. *Phys. Rev. Research* **5**, 033131 (2023).
- [S9] Baumgartner, C. *et al.* Effect of Rashba and Dresselhaus spin–orbit coupling on supercurrent rectification and magnetochiral anisotropy of ballistic Josephson junctions. *Journal of Physics: Condensed Matter* **34**, 154005 (2022).
- [S10] Clem, J. R. Josephson junctions in thin and narrow rectangular superconducting strips. *Phys. Rev. B* **81**, 144515 (2010).
- [S11] Banerjee, A. *et al.* Phase asymmetry of Andreev spectra from Cooper-pair momentum. *Phys. Rev. Lett.* **131**, 196301 (2023).
- [S12] Yuan, N. F. Q. & Fu, L. Supercurrent diode effect and finite-momentum superconductors. *Proc. Natl. Acad. Sci. USA* **119**, e2119548119 (2022).
- [S13] Davydova, M., Prembabu, S. & Fu, L. Universal Josephson diode effect. *Sci. Adv.* **8**, eabo0309 (2022).